The Journal of Clinical Investigation

MEK inhibitor Mirdametinib promotes fracture healing in osteofibrous dysplasia RASopathy

Aysha Khalid, Kristin Denton, Nandina Paria, Ila Oxendine, Meghan Wassell, Reuel Cornelia, Sasidhar Uppuganti, Jeffry S. Nyman, G. Jayashree Jagadeesh, Carlos R. Ferreira, Simon J. Conway, Robert E. Hammer, John O. Ritter, Mylinh Nguyen, David A. Podeszwa, Laura J. Klesse, Carol A. Wise, Jonathan J. Rios

J Clin Invest. 2026. https://doi.org/10.1172/JCI199048.

Research In-Press Preview **Bone biology** **Clinical Research** **Genetics**

Osteofibrous dysplasia (OFD) is a skeletal RASopathy presenting with periosteal bone lesions that may progress to fracture and delayed healing (pseudarthrosis). *MET* gene mutations reducing ubiquitin-mediated protein degradation via loss of the juxtamembrane domain ($\text{MET}^{\Delta \text{JMD}}$) were previously identified in OFD patients, resulting in ligand-dependent gain-of-function. The impact of $MET^{\Delta JMD}$ expression on skeletal progenitor cell differentiation and the potential efficacy of targeted therapies remain unclear. We engineered $Met^{\Delta JMD}$ mice and showed that $Met^{\Delta JMD}$ expression inhibited osteogenic differentiation of skeletal progenitor cells in vitro and impaired cortical bone development and reduced bone stiffness in vivo. In contrast, conditional deletion of *Met* enhanced osteogenic differentiation of periosteal progenitor cells. Inhibition of MAPK signaling with MEK inhibitors restored osteogenic differentiation of mouse $Met^{\Delta JMD}$ skeletal progenitor cells and promoted activation of transcriptional signatures associated with skeletal development and osteoblast differentiation in OFD patient pseudarthrosis-derived primary cells. With this preclinical support, we treated with the MEK inhibitor mirdametinib a pediatric OFD patient suffering from a 3-year history of persistent pseudarthrosis, resulting in fracture union. Our findings demonstrate a bi-directional role for MET in regulating osteogenic differentiation of skeletal progenitor cells and a therapeutic avenue to improve clinical outcomes for this, and potential other, skeletal RASopathies.

MEK inhibitor Mirdametinib promotes fracture healing in osteofibrous dysplasia RASopathy

Aysha Khalid[1], Kristin Denton[1], Nandina Paria[1], Ila Oxendine[1], Meghan Wassell[1], Reuel Cornelia[1], Sasidhar Uppuganti[2], Jeffry S. Nyman[2,3,4], G. Jayashree Jagadeesh[5], Carlos R. Ferreira[5], Simon J. Conway[6], Robert E. Hammer[7], John Ritter[7], Mylinh Nguyen[7], David A. Podeszwa[8,9], Laura J. Klesse[10,11,12], Carol A. Wise[1,9,10,13], Jonathan J. Rios[1,9,10,11,13,*]

[1]Center for Translational Research, Scottish Rite for Children, Dallas, TX, USA

[2]Department of Orthopaedic Surgery, Vanderbilt University Medical Center, Nashville, TN, USA

[3]Department of Biomedical Engineering, Vanderbilt University, Nashville, TN, USA

[4]United States Department of Veterans Affairs, Tennessee Valley Healthcare System, Nashville, TN, USA

[5]Unit on Skeletal Genomics, *Eunice Kennedy Shriver* National Institute of Child Health and Human Development, National Institutes of Health, Bethesda, MD, USA

[6]Herman B. Wells Center for Pediatric Research, Indiana University School of Medicine, Indianapolis, IN, USA

[7]Department of Biochemistry, UT Southwestern Medical Center, Dallas, TX, USA

[8]Department of Orthopaedics, Scottish Rite for Children, Dallas, TX, USA

[9]Department of Orthopaedic Surgery, UT Southwestern Medical Center, Dallas, TX, USA

[10]Department of Pediatrics, UT Southwestern Medical Center, Dallas, TX, USA

[11]Simmons Comprehensive Cancer Center, UT Southwestern Medical Center, Dallas, TX, USA

[12]Department of Pediatrics, Children's Health, Dallas, TX, USA

[13]McDermott Center for Human Growth and Development, UT Southwestern Medical Center, Dallas, TX, USA

*Corresponding author: Jonathan J Rios
Scottish Rite for Children
2222 Welborn Street
Dallas, Texas 75219
(E) Jonathan.Rios@tsrh.org
(P) +1 214-559-7877

The authors have declared that no conflict of interest exists.

ABSTRACT

Osteofibrous dysplasia (OFD) is a skeletal RASopathy presenting with periosteal bone lesions that may progress to fracture and delayed healing (pseudarthrosis). *MET* gene mutations reducing ubiquitin-mediated protein degradation via loss of the juxtamembrane domain (MET$^{\Delta JMD}$) were previously identified in OFD patients, resulting in ligand-dependent gain-of-function. The impact of *MET*$^{\Delta JMD}$ expression on skeletal progenitor cell differentiation and the potential efficacy of targeted therapies remain unclear. We engineered *Met*$^{\Delta JMD}$ mice and showed that *Met*$^{\Delta JMD}$ expression inhibited osteogenic differentiation of skeletal progenitor cells in vitro and impaired cortical bone development and reduced bone stiffness in vivo. In contrast, conditional deletion of *Met* enhanced osteogenic differentiation of periosteal progenitor cells. Inhibition of MAPK signaling with MEK inhibitors restored osteogenic differentiation of mouse *Met*$^{\Delta JMD}$ skeletal progenitor cells and promoted activation of transcriptional signatures associated with skeletal development and osteoblast differentiation in OFD patient pseudarthrosis-derived primary cells. With this preclinical support, we treated with the MEK inhibitor mirdametinib a pediatric OFD patient suffering from a 3-year history of persistent pseudarthrosis, resulting in fracture union. Our findings demonstrate a bi-directional role for MET in regulating osteogenic differentiation of skeletal progenitor cells and a therapeutic avenue to improve clinical outcomes for this, and potential other, skeletal RASopathies.

INTRODUCTION

Osteofibrous dysplasia (OFD; MIM#:607278) is a congenital skeletal disorder affecting the long bones of children (1). OFD is defined by radiolucent lesions at the periosteal surface affecting the cortical bone. Lesions are often focal, though multi-focal involvement of the same bone has been observed. OFD lesions may also be associated with bowing and pathologic fracture that may fail to heal and develop a persistent pseudarthrosis. While OFD is most often sporadic and unilateral, families with inherited OFD as well as rare cases of bilateral OFD have been described (2-5). Histologic diagnosis of OFD is characterized by osteoblast rimming of woven bone with a central fibrous osteolytic nidus, which distinguishes OFD from other conditions, such as fibrous dysplasia. Some OFD lesions may resolve spontaneously; however, surgical *en bloc* excision may be needed for progressive lesions or for persistent fracture pseudarthrosis (6).

The MET proto-oncogene receptor tyrosine kinase (RTK) protein consists of an extracellular domain, a transmembrane region, a juxtamembrane domain (JMD), and a kinase domain. Phosphorylation sites within the JMD and kinase domains negatively and positively regulate MET activity, respectively. Activation of the MET receptor requires binding of its ligand, hepatocyte growth factor (HGF), which leads to phosphorylation of kinase domain tyrosine residues, protein internalization, and activation of downstream effector pathways such as the RAS/RAF/MEK/ERK (MAPK), the PIK3CA/AKT/mTOR, and STAT pathways, among others (7-11). After the initiation of this signaling cascade, the receptor is recycled back to the cell surface or undergoes ubiquitin-mediated degradation via phosphorylation of the JMD tyrosine residue (Tyr_{1003}) by the CBL ubiquitin ligase.

Inherited and somatic pathogenic *MET* gene variants were previously identified in OFD patients with familial and sporadic disease, respectively (4). Inherited variants were localized to the exon 14 splice donor site, which resulted in exon skipping and in-frame exclusion of the JMD in an otherwise full-length protein. To date, the only somatic OFD variant detected was a point mutation at the Tyr_{1003} residue within the JMD. Splice exclusion of the JMD or mutation of the Tyr_{1003} residue leads to loss of ubiquitin-mediated degradation of the receptor and prolonged pathway activation (4, 10). Therefore, OFD-causing variants lead to a ligand-dependent gain-of-function MET receptor, as has been described in human cancers (12).

The molecular context of $MET^{\Delta \mathrm{JMD}}$ expression is best demonstrated in cancer, where it promotes tumor growth via an "oncogene addiction" mechanism (13). Inhibition of the addicted pathway results in cancer cell death, and consequently MET inhibitors were approved to treat non-small cell lung cancer (NSCLC) associated with $MET^{\Delta \mathrm{JMD}}$ expression (14, 15). However, the impact of $MET^{\Delta \mathrm{JMD}}$ expression on skeletal progenitor cell differentiation or skeletal development remains unstudied, and thus no evidence yet exists regarding the use of targeted therapies to treat the OFD RASopathy.

Here, we demonstrate that Met bi-directionalally regulates osteogenic differentiation, in part, via regulation of MAPK signaling. Inhibition of MAPK signaling with MEK inhibitors rescued osteogenic differentiation of skeletal progenitor cells from $Met^{\Delta \mathrm{JMD}}$ mice and promoted expression of osteogenic gene signatures in OFD patient pseudarthrosis-derived primary cells. Finally, we present the successful treatment of a long-term persistent pseudarthrosis in an OFD patient with the MEK inhibitor mirdametinib. Results from our study support the potential use of MEK inhibitors to treat pseudarthrosis associated with OFD and, potentially, other RASopathies.

RESULTS

Met$^{\Delta JMD}$ expression promotes Erk pathway activation in skeletal progenitor cells

To investigate the impact of *Met*$^{\Delta JMD}$ expression on skeletal progenitor cell differentiation and skeletal development, we deleted the JMD-encoding *Met* exon 15 in mice using CRISPR/Cas9 (Supplemental Figure 1A). Heterozygous *Met*$^{+/\Delta JMD}$ mice (herein referred to as *Met*$^{\Delta JMD}$) were viable and fertile with no overt phenotype. Similar to mice harboring constitutive activating *Met* kinase domain variants (16), homozygous *Met*$^{\Delta JMD/\Delta JMD}$ mice were embryonic lethal. Ligand-dependent gain-of-function due to loss of the MET JMD in lung cancer cell lines results in prolonged MAPK pathway activation following stimulation with HGF (17). Therefore, we isolated bone marrow stromal cells (BMSCs) from adult control and *Met*$^{\Delta JMD}$ mice, treated cells with HGF, and quantified relative Erk activation and normalization. In both control and *Met*$^{\Delta JMD}$ BMSCs, the Erk pathway was quickly activated in response to HGF, though normalization following stimulation was significantly delayed in *Met*$^{\Delta JMD}$ BMSCs compared to control (Figure 1, A and B). Thus, *Met*$^{\Delta JMD}$ mice harbor a heterozygous germline deletion of the endogenous *Met* JMD-encoding exon leading to ligand-dependent gain-of-function in MAPK signaling.

OFD lesions occur at the periosteal surface of bone, and *Met* expression was previously detected at the periosteal surface of mouse embryonic long bones (4). Therefore, we cultured Leptin receptor (*LepR*)-expressing BMSCs and Periostin (*Postn*)-expressing periosteal explant cells (PECs) from control and *Met*$^{\Delta JMD}$ mice (Supplemental Figure 1, B and C) and tested expression of *Met* and *Hgf* in both cell types. *Met* expression was significantly higher in PECs compared to BMSCs ($p<0.0001$). Compared to control cells, *Met* expression was higher in *Met*$^{\Delta JMD}$ BMSCs and PECs (Figure 1C). This difference was predominantly due to the relative over-expression of the *Met*$^{\Delta JMD}$ allele (Supplemental Figure 1, D and E), implicating, for the first time, an allele-specific feedback mechanism associated with the *Met*$^{\Delta JMD}$ allele. While *Hgf* expression was modestly elevated in *Met*$^{\Delta JMD}$ BMSCs compared to control, *Hgf* expression was significantly higher in PECs from both control and *Met*$^{\Delta JMD}$ mice (Figure 1D). Consistent with the higher *Met* and *Hgf* expression in PECs, Erk activation was significantly higher in serum-starved control and *Met*$^{\Delta JMD}$ PECs compared to BMSCs (Figure 1, E and F). No differences were observed in AKT/mTOR pathway activation as assayed by phospho-S6 (Supplemental Figure 1F). These results implicate a molecular basis for the periosteal localization of OFD lesions observed in patients.

Lastly, MET activation enhances tumor growth and invasion, in part, through promoting the epithelial-to-mesenchymal transition (18-21). Therefore, we tested cell adhesion and the expression of mesenchymal cell adhesion-associated genes in control and *Met*$^{\Delta JMD}$ PECs. Compared to control cells, *Met*$^{\Delta JMD}$ PECs demonstrated significantly greater adherence in culture concomitant with significantly higher expression of the cell adhesion genes N-cadherin (*Ncad*) and vimentin (*Vim*) (Figure 1, G-I), though no difference in cell proliferation was observed (Supplemental Figure 1, G and H). Taken together, these results demonstrate molecular and cellular defects in skeletal progenitor cells from *Met*$^{\Delta JMD}$ mice associated with ERK pathway activation.

Impaired progenitor cell differentiation and skeletal development in *Met*$^{\Delta JMD}$ mice

In osteoprogenitor cells, MAPK homeostasis is essential for proper osteogenic differentiation and mineralization. Pre-clinical cellular and rodent models of skeletal RASopathies, such as in Neurofibromatosis Type 1 (NF1) (22, 23) and others (24), have implicated impaired osteogenic differentiation and/or mineralization in the pathogenesis of disease. Therefore, we tested osteogenic differentiation of *Met*$^{\Delta JMD}$ PECs by measuring the relative expression of early and late osteogenic genes following differentiation, including integrin binding sialoprotein (*Ibsp*), RUNX family transcription factor 2 (*Runx2*), osterix (*Osx*), osteocalcin (*Ocn*), and dentin matrix acidic phosphoprotein 1 (*Dmp1*). While expression of all osteogenic genes was significantly increased in control PECs following differentiation, expression of these genes was mostly unchanged in *Met*$^{\Delta JMD}$ PECs, suggesting impaired osteogenic differentiation in *Met*$^{\Delta JMD}$ PECs (Figure 2, A and B, Supplemental Figure 2, A-C). Consistent with this, mineralization measured by Alizarin staining was significantly reduced following differentiation of *Met*$^{\Delta JMD}$ PECs compared to control (Figure 2, C and D). These results demonstrate expression of the *Met*$^{\Delta JMD}$ allele impairs osteogenic differentiation and mineralization of periosteal osteoprogenitor cells, potentially due to MAPK activation.

To evaluate whether in vitro defects in osteoblast differentiation and mineralization correlate with skeletal deficiencies in vivo, we analyzed the microstructure and biomechanical properties of the long bones from adult control and *Met*$^{\Delta JMD}$ mice. The trabecular bone microarchitecture was unchanged in *Met*$^{\Delta JMD}$ mice compared to control (Supplemental Figure 2, D-G), and no differences were observed in surface osteoblast and osteoclasts between control and *Met*$^{\Delta JMD}$ mice (Supplemental Figure 2, H and I). In contrast, cortical porosity, but not cortical thickness, was significantly increased at the femur mid-diaphysis in *Met*$^{\Delta JMD}$ mice, with greater differences observed in male compared to female mice (Figure 2, E and F). The polar Moment of Inertia (pMOI) of the femur mid-diaphyseal cortex, a structural parameter sensitive to the periosteal circumference, was lower in 4-month-old male *Met*$^{\Delta JMD}$ mice (Figure 2G). Likewise, both the periosteal and endosteal circumferences were reduced in male *Met*$^{\Delta JMD}$ mice

(Figure 2, H and I). Consistent with increased cortical porosity, biomechanical testing further demonstrated reduced stiffness and post-yield toughness (PYT) in the femurs of male *Met*$^{\Delta JMD}$ mice compared to control (Figure 2, J and K). Taken together, *Met*$^{\Delta JMD}$ expression inhibits osteogenic differentiation of periosteal progenitor cells, resulting in impaired cortical bone development in mice leading to decreased resistance to an applied load.

OFD lesions may progress to fracture, which is often treated with recombinant bone morphogenetic protein 2 (BMP2) applied to the outer periosteal bone surface. Therefore, we tested whether exogenous BMP2 may rescue osteogenic differentiation defects inherent in *Met*$^{\Delta JMD}$ PECs. Osteogenic gene expression was significantly increased following osteogenic differentiation with BMP2 of both control and *Met*$^{\Delta JMD}$ PECs (Figure 2, L and M, Supplemental Figure 2, J-L). Alizarin staining confirmed rescue of osteoblast mineralization following differentiation of *Met*$^{\Delta JMD}$ PECs with BMP2 (Figure 2, N and O). These results demonstrate that *Met*$^{\Delta JMD}$-expressing skeletal progenitor cells remain responsive to the anabolic effects of BMP2 despite activated MAPK signaling. The intact responsiveness to BMP2 is consistent with the lack of overt skeletal deformity in *Met*$^{\Delta JMD}$ mice.

Reduced *Met* expression enhances osteogenic differentiation of PECs

Met$^{\Delta JMD}$ expression significantly inhibits osteogenic differentiation of PECs; therefore, we next tested whether loss of *Met* promotes PEC osteogenesis. To test this, we cultured PECs following conditional deletion of *Met* in the bone periosteum of *Postn*-cre;*Met*$^{flox/flox}$ mice (herein called *Met*^{Postn}). Expression of *Met*, and to a lesser extent *Hgf*, was significantly reduced in *Met*^{Postn} PECs compared to control (Figure 3, A and B). To test osteogenic differentiation, we measured the expression of the osteogenic genes *Dmp1* and *Alpl* in control and *Met*^{Postn} PECs.

Following differentiation, the expression of osteogenic genes was significantly higher in *Met*$^{\text{Postn}}$ PECs compared to differentiated control PECs (Figure 3, C-F). Likewise, there was suggestive evidence (p=0.08) for increased mineralization following differentiation of *Met*$^{\text{Postn}}$ PECs compared to control (Figure 3, G and H). Taken together with results from *Met*$^{\Delta\text{JMD}}$ PECs, these results suggest Met regulates osteogenic differentiation of cultured PECs and that inhibition of Met, or downstream MAPK signaling, may rescue osteogenic differentiation of *Met*$^{\Delta\text{JMD}}$ PECs.

Mek inhibition rescues differentiation and mineralization of *Met*$^{\Delta\text{JMD}}$ PECs

The elevated MAPK activation associated with *Met*$^{\Delta\text{JMD}}$ expression implicates the use of targeted therapies, such as the MET inhibitor (METi) capmatinib or the MEK inhibitors (MEKi) mirdametinib and selumetinib, to treat OFD (Figure 4A). Each compound was tested for its ability to rescue the cell adhesion and osteogenic differentiation defects inherent in *Met*$^{\Delta\text{JMD}}$ PECs. Capmatinib is approved by the US Food and Drug Administration (FDA) to treat lung cancers expressing the *MET*$^{\Delta\text{JMD}}$ allele or with high *MET* copy number (copy number >10), both of which convey the MET oncogene addiction (14, 25). In contrast, MET inhibition was ineffective in treating lung cancer with low-level *MET* amplification (copy number <10) (14). These results suggest efficacy of MET inhibitors is context dependent, and the effectiveness of MET inhibition in OFD remains untested. As expected, cell adhesion of vehicle-treated *Met*$^{\Delta\text{JMD}}$ PECs was significantly higher compared to vehicle-treated control cells, while capmatinib treatment significantly reduced cell adhesion of *Met*$^{\Delta\text{JMD}}$ PECs to control levels (Supplemental Figure 3A). Likewise, expression of the cell adhesion genes *Ncad* and *Vim* were significantly increased in vehicle-treated *Met*$^{\Delta\text{JMD}}$ PECs but normalized to control levels with capmatinib treatment (Supplemental Figure 3, B and C). To test mineralization, control and *Met*$^{\Delta\text{JMD}}$ PECs were treated with capmatinib throughout in vitro osteogenic differentiation. Following osteogenic differentiation, capmatinib failed to rescue mineralization of *Met*$^{\Delta JMD}$ PECs (Supplemental Figure 3, D and E). These results suggest that, unlike in MET-addicted lung cancer, the expression of *Met*$^{\Delta JMD}$ in PECs is not sufficient to permit therapeutic rescue with a METi. In support of this, the level of *Met* expression in *Met*$^{\Delta JMD}$ PECs is 5-times lower than in METi-sensitive sarcomas expressing the *Met*$^{\Delta JMD}$ allele (Jonathan J. Rios, SRC, Dallas, Texas, USA, unpublished observation).

We next tested whether directly targeting MAPK pathway activation with the MEKi mirdametinib rescues osteogenic differentiation and mineralization of *Met*$^{\Delta JMD}$ PECs. Mirdametinib (PD0325901) is a non-ATP-competitive and selective small-molecule inhibitor of both MEK1 and MEK2 phosphorylation (26). In adults and children with NF1, mirdametinib reduced plexiform neurofibroma (pNF) tumor volume, leading to its recent approval by the FDA and the European Medicines Agency (27). To confirm the molecular response of *Met*$^{\Delta JMD}$ PECs to mirdametinib treatment, we compared MAPK pathway activation of treated cells to vehicle-treated *Met*$^{\Delta JMD}$ PECs. Compared to vehicle treatment, mirdametinib significantly reduced ERK pathway activation in *Met*$^{\Delta JMD}$ PECs (Figure 4, B and C). Mirdametinib rescued cell adhesion of treated *Met*$^{\Delta JMD}$ PECs, which was further confirmed with the significant reduction in expression of *Ncad* and *Vim* (Figure 4, D-F). We next tested rescue of osteogenic differentiation and mineralization with mirdametinib treatment. Compared to vehicle, mirdametinib treatment significantly rescued osteogenic differentiation of *Met*$^{\Delta JMD}$ PECs, as evidenced by increases in the expression of osteogenic genes (Figure 4, G-I, Supplemental Figure 4, A-C). Consistent with the rescue in differentiation, mirdametinib also significantly rescued mineralization in differentiated *Met*$^{\Delta JMD}$ PECs (Figure 4, J and K).

To ensure rescue of cell adhesion, osteogenic differentiation, and mineralization of *Met*$^{\Delta JMD}$ PECs was associated with MAPK pathway inhibition, we independently repeated all experiments with selumetinib, another MEKi FDA approved to treat pNF in children with NF1 (28). As expected, selumetinib significantly reduced ERK pathway activation in *Met*$^{\Delta JMD}$ PECs (Supplemental Figure 5, A and B) and rescued expression of cell adhesion genes *Ncad* and *Vim* (Supplemental Figure 5, C and D). Compared to vehicle-treated cells, selumetinib treatment throughout differentiation resulted in significantly increased expression of osteogenic genes, consistent with rescue of osteogenesis (Supplemental Figure 5, E-J). Finally, Alizarin staining demonstrated significant rescue of mineralization of selumetinib-treated *Met*$^{\Delta JMD}$ PECs (Supplemental Figure 5, K and L). These results demonstrate inhibition of MEK pathway activation rescues cellular and osteogenic defects inherent in *Met*$^{\Delta JMD}$ PECs and further suggest a therapeutic potential for MEKi in children with OFD.

MEKi enhances the expression of skeletal gene signatures in OFD patient-derived primary cells

We previously identified a somatic p.(Tyr1003Ser) variant in primary cells cultured from a patient OFD fracture lesion, implicating somatic *MET* mutations in the pathogenesis of sporadic OFD-associated pseudarthrosis (4). To further evaluate somatic *MET* mutations as a cause of OFD fracture pseudarthrosis, we tested *MET*$^{\Delta JMD}$ expression by RT-PCR and sequenced the JMD-encoding exon for Tyr$_{1003}$ mutations in primary cells cultured from pseudarthroses of four OFD patients. RT-PCR detected an alternatively spliced *MET* transcript in lesion-derived primary cells from one patient (Supplemental Figure 6A). No alternative splicing or MET JMD or kinase domain mutations were detected in the remaining three patient samples, possibly due to somatic mosaicism below the level of detection or due to mutations present in other genes not previously associated with OFD. The alternatively spliced variant was cloned and confirmed by Sanger sequencing as the *MET*$^{\Delta JMD}$ allele (Supplemental Figure 6B). Sequencing of DNA from lesion-derived primary cells identified a somatic c.3028+2T>C splice donor variant that was not detected in DNA from a blood sample from the patient (Supplemental Figure 6C). The same allele was previously reported as a somatic mutation in lung adenocarcinomas (29, 30). We performed droplet digital PCR to confirm and quantify the mutation using DNA from primary lesion cells and blood (control). The mutation burden (variant allele fraction) was 19% in the lesion-derived cells but was undetected in the blood sample (Supplemental Figure 6D), further confirming the somatic occurrence of this variant resulting in expression of the *MET*$^{\Delta JMD}$ allele. These results independently confirm that somatic *MET* mutations of the JMD domain are a cause of sporadic OFD and raise the possibility that mutations in other genes may also contribute to OFD.

To begin investigating the therapeutic potential of METi or MEKi for the treatment of OFD, we tested the impact of METi or MEKi monotherapy on OFD lesion-derived primary cells, including patients with and without detectable *MET* mutations. We first tested the molecular impact of the METi capmatinib on patient lesion-derived primary cells. Capmatinib treatment failed to significantly inhibit ERK pathway activation, and RNAseq analysis demonstrated a minimal molecular response to METi, with few genes differentially expressed compared to vehicle treatment (Supplemental Figure 7, A-C, Supplemental Table 1). As with the *Met*$^{\Delta JMD}$ PECs, these results do not support a therapeutic potential for METi in OFD.

We next tested the response of OFD patient lesion-derived primary cells to MEKi, including from patients with and without detectable *MET* gene variants. Mirdametinib significantly, and in a dose-dependent manner, inhibited ERK pathway activation (Figure 5, A and B). RNA-seq profiling distinguished vehicle-treated from mirdametinib-treated samples, identifying 333 transcripts with reduced expression and 152 transcripts with increased expression following mirdametinib treatment (Figure 5, C-E, Supplemental Table 2). We performed gene ontology (GO) analysis to summarize the biologic response of mirdametinib on OFD lesion-derived primary cells. GO analysis results demonstrated that genes with increased expression following mirdametinib treatment were significantly associated with biologic processes required for skeletal development and fracture healing (Figure 5F, Supplemental Table 3). Genes with reduced expression following treatment were significantly enriched in MAPK pathway processes as well as biologic processes expected to be affected by MAPK pathway inhibition, such as cell cycle regulation and cell proliferation (Figure 5G, Supplemental Table 4). These results are similar to a recent study of NF1 patient pseudarthrosis-derived primary cells treated with the MEKi selumetinib, which demonstrated the molecular response to treatment was specific to MAPK hyper-active primary lesion cells, while patient-matched iliac crest control primary cells showed minimal response to treatment (31).

To further demonstrate the molecular response of OFD lesion-derived primary cells to ERK pathway inhibition, we similarly tested the effects of selumetinib. ERK pathway activation was significantly reduced with selumetinib treatment (Supplemental Figure 7A). Transcriptome profiling distinguished selumetinib- from vehicle-treated cells and identified 581 transcripts with reduced expression and 331 transcripts with increased expression following selumetinib treatment (Supplemental Figure 7, B, D, and E, Supplemental Table 5). Similar to mirdametinib, genes with increased expression following selumetinib treatment were associated with extracellular matrix formation and osteoblast differentiation, while genes with reduced expression were associated with MAPK pathway and kinase activity processes (Supplemental Figure 7, F and G, Supplemental Table 6 and 7). For all treatments, no differences were observed between patients with (n=2) and without (n=3) detectable *MET* mutations. Taken together, these results provide molecular evidence implicating MEKi as a potential therapeutic strategy to promote bone healing in patients with OFD.

Mirdametinib promotes fracture healing in an OFD patient

Results utilizing *Met*$^{\Delta JMD}$ PECs and primary cells from OFD patients suggested MEKi may provide therapeutic benefit for children with OFD-associated pseudarthrosis. MEKi have become more widely utilized in the pediatric population for several indications where the MAPK pathway is hyper-activated and have demonstrated safety and tolerability. Two MEKi resulted in inhibition of ERK pathway activation in OFD patient primary cells and increased expression of genes and pathways known to promote bone formation and/or fracture healing. Therefore, we hypothesized that monotherapy with a MEKi together with standard-of-care surgical treatment may promote healing of OFD-associated pseudarthrosis.

Given the strong preclinical data, we treated with the MEKi mirdametinib a patient with OFD who, after multiple attempts at surgical correction, had a persistent pseudarthrosis. The patient initially presented at 1 year of age with a tibia lesion requiring resection, which resulted in persistent pseudarthrosis. The patient underwent six subsequent surgeries over the next three years due to persistent non-healing. Multiple techniques were utilized to attempt to achieve bone union, including resection, external fixation, iliac crest graft, and application of BMP2, though each revision failed to achieve durable union, and pseudarthrosis persisted (Figure 5H). Local bone infection was assessed for and excluded as a cause of non-union. Biopsy confirmed an OFD diagnosis, though no *MET* gene mutation was identified in cultured lesion-derived primary cells from the patient. Given the molecular response of patient pseudarthrosis-derived primary cells to MEKi in vitro, we sought approval to treat the patient with a MEKi. After appropriate regulatory review and approval from the SpringWorks Therapeutics Compassionate Use Program, the FDA, and the institutional review board at UT Southwestern Medical Center, the family provided consent to the use of mirdametinib. Twelve days after revision surgery that again included resection, external fixation, iliac crest grafting, and BMP2, the patient was started on mirdametinib at a dose of 1 mg twice daily via the dispersible tablet with the standard schedule of 21 days on drug, 7 days off per 28 day cycle. Prior to dosing, the patient underwent baseline ophthalmology evaluation, echocardiogram, physical examination, and laboratory evaluation. The patient has been monitored on-therapy with follow-up evaluations including physical, laboratory, and cardiac evaluations. The patient has tolerated the therapy with no significant toxicity and has only noted grade 1 diarrhea in the first month of therapy that resolved by the second month of therapy. The patient has now completed seven months of therapy with no further toxicity noted.

Fracture healing was monitored by monthly radiographs, which demonstrated progressive maturation of the iliac crest graft that, at 6 months post-surgery, resulted in a durable bony bridge and union of the fracture despite early post-surgical distal segment translation leaving a residual angular deformity (Figure 5I). The external fixator frame was removed and the patient was transitioned to a long leg cast to promote further healing and remodeling and is continuing mirdametinib therapy. Following six prior revision surgeries that resulted in persistent pseudarthrosis, the addition of mirdametinib to standard surgical approaches in this OFD patient resulted in the first bone union. Overall, our preclinical results as well as the single patient reported here demonstrate evidence that MEKi monotherapy together with standard-of-care surgical approaches can result in healing of persistent pseudarthrosis in patients with the OFD RASopathy.

DISCUSSION

In this report, we engineered an OFD mouse model expressing the *Met*$^{\Delta JMD}$ allele to demonstrate the reduced osteogenic potential of periosteal progenitor cells associated with activation of the MAPK pathway. In patients, OFD lesions are restricted to the bone periosteum. Our results implicate the mesenchymal niche-specific expression of *Met* and *Hgf*, encoding the only known ligand for the MET receptor, in the restricted clinical presentation of bony lesions to the periosteum. In vivo, expression of the *Met*$^{\Delta JMD}$ allele was associated with cortical long bone defects in mice, as are observed in human patients (32), including less structural resistance to torsion and more cortical porosity. These results are consistent with impaired differentiation and mineralization associated with MAPK activation in the bone periosteum, recapitulating the human condition.

OFD is one of multiple somatic skeletal diseases, including NF1 (33, 34), Melorheostosis (35), and others, associated with hyperactive RAS (i.e., RASopathies) or downstream MAPK signaling. These conditions are associated with different skeletal presentations, some of which may predispose to pathologic fracture and subsequent pseudarthrosis. Fractures are often treated with rigid fixation and a BMP2-collagen graft to promote bone healing, though clinical and pre-clinical studies suggest MAPK hyper-activation inhibits the osteoanabolic effects of BMP2 (36-39). Surprisingly, our results demonstrate that despite ERK pathway activation, BMP2 was sufficient to rescue osteogenic differentiation of *Met*$^{\Delta JMD}$ osteoprogenitor cells in vitro. These results suggest the therapeutic efficacy of BMP2 differs between skeletal RASopathies despite their mechanistic convergence on hyperactive MAPK signaling. Further studies of these signaling pathways may uncover a mechanistic basis for this divergent osteogenic response to BMP2.

In cancer, *MET*$^{\Delta\text{JMD}}$ expression leads to an oncogene addiction, which is described as a molecular switch rendering cells dependent on a singular signal transduction pathway, thereby sensitizing tumors to compounds targeting these pathways. In addition to *MET*$^{\Delta\text{JMD}}$ expression, high copy number amplification of the *MET* gene also leads to oncogene addiction; however, MET inhibitors are only therapeutically effective with *MET* copy number at least 10 or greater (14, 15). These results suggest that the response to MET inhibitors is dependent on the degree to which persistent *MET* expression sustains the activation of downstream signaling pathways and to the degree to which cellular dysfunction is dependent on this signaling. It remains possible, as with low-level *MET* amplification, that feedback or other mechanisms may sustain the activation of downstream pathways without inducing an addiction phenotype. Indeed, our results demonstrate, both in mouse and human primary cells, that MET inhibition does not reverse the cellular and molecular consequences of *MET* expression in OFD. Thus, while mutations resulting in *MET*$^{\Delta\text{JMD}}$ expression are known to cause OFD, an oncogene addiction-like phenotype is not evident in *Met*$^{\Delta\text{JMD}}$-expressing mouse skeletal progenitor cells or in OFD patient lesion-derived primary cells. These results are consistent with a lack of transformation or increased cancer risk in OFD patients with somatic or inherited *MET* mutations (1, 4).

In contrast to MET inhibition, directly targeting downstream MEK signaling with the MEKis mirdametinib or selumetinib rescued osteogenic differentiation and mineralization of *Met*$^{\Delta\text{JMD}}$ mouse osteoprogenitor cells. Likewise, MEKi reversed the molecular signatures inherent in OFD patient lesion-derived primary cells, including from patients with and without detectable *MET* mutations. Both mirdametinib and selumetinib are approved for use in children as young as 2 years of age for the treatment of pNF and may potentially be repurposed to treat conditions associated with hyper-active MAPK signaling, such as OFD. As part of a compassionate use protocol, we demonstrate the successful healing of a persistent pseudarthrosis in a young child with OFD. Following 6-months on-treatment, the therapy was well tolerated and resulted in radiographic evidence of union sufficient to transition from rigid external fixation to cast. Based on this result, we hypothesize that post-operative MEKi may support pseudarthrosis healing and that treatment could potentially be discontinued upon satisfactory healing. Future studies will be required to determine appropriate outcomes for discontinuation.

Results from this study demonstrate a non-surgical therapeutic opportunity for the treatment of OFD in children, opening future potential for similar studies or treatment in patients with other RASopathy-associated skeletal disease. As with OFD, patients with NF1 are at increased risk of pathologic fracture and subsequent pseudarthrosis that often does not heal despite use of BMP2 and requiring amputation (36). As well, melorheostosis presents with periosteal bone lesions and is caused by activating somatic variants in the gene encoding MEK1 (35). Therefore, our results, together with observations in other RASopathies, converge to implicate MEK inhibition as an effective treatment across a spectrum of somatic skeletal RASopathies.

METHODS

Sex as a biological variable.

For human studies, sex was not considered as a biological variable. For mouse studies, both male and female animals were included, and findings are reported for both sexes.

Generation of *Met*$^{\Delta JMD}$ and *Met*^{Postn} mice.

Met$^{\Delta JMD}$ mice were generated using CRISPR/Cas9 reagents at the Transgenic Technology Center of UT Southwestern Medical Center. The sgRNAs were designed to target the intron upstream (GCACTGGGTCAAAGTCTCCT) and downstream (CACCAGACCGACAAATGGTC) of the JMD-encoding exon 15. crRNA and tracRNA were annealed and mixed with Cas9 protein nuclease from IDT to form a ribonucleotide protein complex. Cas9 (25ng/ul) and each sgRNA (25ng/ul) was microinjected into the pronucleus of fertilized one-cell eggs isolated from superovulated females C57BL/6J. The eggs were incubated in media containing cytochalasin-B immediately before and during microinjection to improve egg survival. The surviving eggs were transferred into the oviducts of day 0.5 pseudopregnant recipient ICR females (Envigo, Inc.) to produce founder mice. Founder mice were genotyped by Sanger sequencing and a mouse harboring deletion of the exon was outcrossed to C57BL/6 mice for at least 3 generations.

Met^{Postn} mice were generated by first crossing *Postn*-cre (40) mice with *Met*^{flox} (41) (#016974, The Jackson Laboratory, USA) mice. Resulting heterozygous mice were inter-crossed to produce control (without *Postn*-cre or Postn-cre^{+};*Met*$^{+/+}$) and *Met*^{Postn} mice.

All mice were maintained on a C57BL/6 background.

Cell culture and differentiation

BMSC and PEC mesenchymal skeletal progenitor cells were isolated as previously described (42). Hindlimb long bones were dissected and liberated of soft tissues. Epiphyses were removed and BMSCs were flushed and expanded in complete α-MEM media (catalog # 12571-063, Gibco. Thermofisher Scientific, USA) supplemented with 10% FBS (FBS; catalog# A56708-01, Thermo Fisher Scientific, USA) and 1% penicillin/streptomycin (PS; catalog#15140-122, Thermo Fisher Scientific, USA). The flushed bones were plated in α-MEM supplemented with 20% FBS and 1% penicillin/streptomycin and PECs were allowed to migrate out of the explants. Cells were washed with phosphate buffered saline (PBS, catalog# SH30028.02, Hyclone, USA), passaged using Trypsin/EDTA solution (catalog #CC-5012, Lonza, USA), and maintained in α-MEM supplemented with 10% FBS and 1% penicillin/streptomycin. The cells were tested negative for mycoplasma contamination throughout the study.

Osteogenic differentiation was achieved by supplementing the complete α-MEM media with 100ug/mL L-ascorbic acid 2-phosphate (catalog #A92902, Sigma Aldrich, USA) and 5mM β-glycerophosphate (catalog #50020, Sigma Aldrich, USA) for 14 days. Media was refreshed every 3 days. RNA was extracted from cultured cells using TRIzol (catalog #15596018, Thermofisher Scientific, USA). cDNA synthesis was performed using the High Capacity RNA-to-cDNA Kit (catalog #4387406, Thermo Fisher Scientific, USA).

For pharmacologic inhibitor experiments, primary mouse cells were treated with vehicle (DMSO, catalog#D2650, Sigma Aldrich, USA), the MET inhibitor capmatinib (10μM, catalog#S2788, Selleck Chemicals, USA), the MEK inhibitor mirdametinib (1μM, catalog#S1036, Selleck Chemicals, USA), or the MEK inhibitor selumetinib (5μM, catalog#S1008, Selleck Chemicals, USA). For time-course experiments, mouse cells were serum-starved overnight, treated with 1.5nM HGF (catalog#H9661, Sigma Aldrich, USA) for 5 minutes and then media replaced with serum-free α-MEM for the indicated times.

Gene expression of undifferentiated and differentiated samples was evaluated using SYBR Green PCR Master Mix (catalog#4364344, Thermo Fisher Scientific, USA). Primers sequences can be provided upon request. Target specificity was evaluated by melting curve analysis.

Cell staining

Following osteogenic differentiation, the media was removed and the cells were washed once with PBS followed by cell fixation in 50% ethanol for 15 minutes at 4°C and incubated with 1% (wt/vol with 0.1% ammonium hydroxide) Alizarin Red S (catalog #A5533, Sigma Aldrich, USA). The stain was then washed three times with water, dried, and imaged. For quantification, Alizarin Red stain was eluted with 10% cetylpyridinium monohydrate chloride (catalog #190177, MP Biomedical, USA) and the optical density was measured at OD 570nm. For Crystal Violet staining, cells were washed once in PBS at room temperature and incubated with 2% (wt/vol with 0.2% ethanol) Crystal Violet (catalog #C0775, Sigma Aldrich, USA) at room temperature. The stain was washed with water, dried, and imaged. For quantification, Crystal Violet stain was eluted with methanol and optical density was measured at OD 570nm.

Cell cycle analysis

Trypsinized cell suspensions were centrifuged at 300xg for 5 minutes, washed in PBS, and fixed in cold ethanol for 2 hours. Following fixation, cells were pelleted, washed with PBS, and resuspended in propidium iodide (PI) with RNase staining solution (catalogue # ab139418, Abcam, USA) at 37°C for 30 minutes in the dark. Data were acquired using a BD FACSAria^{TM} II and analyzed using BD FACSDiva^{TM} 9.0.1

Histology and quantification

Femurs were fixed in 4% paraformaldehyde overnight and maintained in PBS. Decalcification in 14% EDTA (CAS# 6381-92-6, Sigma Aldrich, USA) and paraffin embedding were performed in the UTSW Histopathology core facility using a Thermo Excelsior Tissue Processor and Sakura TEC6 Embedding Center. Samples were processed with vacuum assist beginning in 70% ethanol followed by 6-graded exchanges of ethanol, 3 exchanges of xylene, and 3 exchanges of molten paraffin. Five-micron sections were cut on a Leica RM2255 rotary microtome. The presence of osteoclasts were identified by Tartrate-Resistant Acid Phosphatase (TRAP) staining. In brief, slides were deparaffinized and rehydrated through multiple xylenes, 100% ethanol, 95% ethanol, and ending in deionized water. To facilitate enzyme activity, slides were incubated in a heated solution containing 0.01% Napthol AS-BI Phosphate Substrate and Basic Stock Incubation Medium. After incubation, slides were directly transferred to a heated solution containing Basic Stock Incubation Medium and Pararosaniline Dye to visualize precipitate from enzyme activity. After sufficient staining, dye development was halted through three five-minute changes of deionized water. Following rinses, sections were then counterstained in a 0.02% Fast Green solution. Excess counterstain was removed by a quick change of deionized water. Tissue sections were then dehydrated and cleared before coverslips were applied with synthetic mounting media.

Paraffin sections for immunohistochemistry were cut 4µm thick, mounted on slides, and dried overnight at 42°C. Selected slides were incubated in 60°C for 10 minutes, deparaffinized in Xylene, rehydrated through descending grade of alcohol (100%,95%70%), and washed in distilled water. Endogenous peroxidase was deactivated with 3% H_20_2 in methanol at room temperature and rinsed with distilled water and transferred to Phosphate Buffer Solution with 0.05% Tween20 (PBST) pH 7.4 (P3563-10PAK, Sigma-Aldrich, USA). Sections were blocked with 10% normal goat serum (catalogue #ab7481, Abcam, USA) for 1 hour at room temperature to reduce non-specific binding and incubated overnight at 4° C with rabbit polyclonal Anti-Sp7/Osterix Antibody (catalogue #ab22552, Abcam, USA) at dilution of 1:10,000. Sections were washed three times with PBST and incubated with secondary antibody goat anti-rabbit IgG HRP conjugate (AP187P, Millipore, USA) at 1:500 dilution for 1 hour and 30 minutes and washed three times in PBST. The chromogen Diaminobenzene (DAB) solution (catalogue #ab64238, Abcam, USA) was placed in sections for 10 minutes to visualize brown reaction and washed in distilled water. Sections were counterstained with Mayer's Hematoxylin (MHS80-2.5L, Sigma-Aldrich, USA) for 2 minutes and washed in running water, dehydrated in ascending grade of alcohol (70%,95%,100%), cleared in Xylene, and mounted in Cytoseal XYL (#8312-4, ThermoScientific, USA). Negative controls were run in parallel by replacing primary antibody with blocking solution.

Slides were scanned using a Motic EasyScan with quantification performed using Motic Digital Slide Assistant software (v.1.0.7.61b).

Patient primary cell culture

Patient-derived primary cells were provided by the Scottish Rite for Children Biorepository. Briefly, patient-derived skeletal specimens were finely chopped and digested in 0.25 mg/ml of collagenase I (catalog#17100017, Thermo Fisher Scientific, USA) and 1 mg/ml of dispase (catalog#17105041, Thermo Fisher Scientific, USA) in Dulbecco's Modified Eagle Medium (catalog#11965092, Thermo Fisher Scientific, USA) supplemented with 15% fetal bovine serum and 1% penicillin/streptomycin (PS) overnight at 37°C. Undigested tissue was removed by centrifugation and the cells were resuspended and plated in α-MEM supplemented with 20% FBS and 1% PS. Primary cells were maintained in α-MEM supplemented with 10% FBS and 1% PS until reaching confluence. Cells were then washed with phosphate buffered saline and passaged using Trypsin/EDTA solution (Catalog #CC-5012, Lonza, USA). The cells were tested for mycoplasma contamination throughout the study. All experiments were performed with early-passage (P<4) cells.

For pharmacologic inhibitor experiments, confluent primary cells were treated with vehicle (DMSO, catalog#D2650, Sigma Aldrich, USA), the MET inhibitor capmatinib (10µM, Catalog# S2788, Selleck Chemicals, USA), the MEK inhibitor mirdametinib (100nM, Catalog# S1036, Selleck Chemicals, USA), or the MEK inhibitor selumetinib (5µM, Catalog# S1008, Selleck Chemicals, USA) for 24 hours.

MET **splicing and variant detection**

Total RNA was extracted from cultured human primary cells using the RNeasy Plus Mini kit (catalog#74134, Qiagen, USA). Cells were washed with PBS two times followed by harvesting with RLT plus buffer from the kit supplemented with beta-mercaptoethanol (catalog#M-7522, Sigma Aldrich, USA). The extraction was performed using manufacture's recommendations. RNA was eluted into 30μl of RNase-free water. cDNA was synthesized by reverse transcription (RT) using the High-Capacity RNA-to-cDNA kit (catalog#4387406, Thermofisher Scientific, USA). Following, RT-PCR was performed to amplify the *MET* transcript and amplicons were resolved by agarose gel electrophoresis. Separated amplicons were excised and extracted from the agarose gel using the QIAquick gel extraction kit (catalog#28704, Qiagen, USA) following manufacturer's recommendations. Sanger sequencing was performed to identify individual amplicon splice variants.

DNA was extracted from whole blood or lesion-derived cultured primary cells using QIAmp DNA extraction kit (catalog#51304, Qiagen, USA) following manufacturer's recommendations. The DNA was used to amplify *MET* exon 14. The amplicons were run on agarose gel to check the correct product size. The amplicons were cleaned up using ExoSAP-IT (catalog#78200200UL, ThermoFisher Scientific, USA) prior to sequencing. Amplicons were then Sanger sequenced to identify potential somatic mutations. Primer sequences are available upon request. The Sanger sequencing data was analyzed using Sequencher V5.1 (Gene Codes Corporations, USA).

Droplet digital PCR (ddPCR)

DNA extracted from blood samples or from primary cells cultured from the lesion bone were analyzed via ddPCR. The assay was ordered using Bio-Rad's online tool for Custom ddPCR assays (Bio-Rad Laboratories, Inc., USA) (assay ID: dHsaMDS847883628). A master mix containing the primers (900 nM), probes (250 nM) for the mutant allele (labeled with FAM) and reference allele (labeled with HEX), the DNA template (200 ng), and 2× ready-to-use ddPCR Supermix (no dUTP) were prepared in a 22ul volume according to the manufacturer guidelines (Bio-Rad, USA). We also added 1µl of HaeIII enzyme to each reaction to improve template accessibility via fragmentation of genomic DNA that is randomly subdivided into droplets that undergo PCR independently.

Droplets generated from the reaction mixture using a QX200 Auto Droplet Generator were amplified using the following PCR cycling protocol: 95°C enzyme activation step for 5 min followed by 40 cycles of a two-step cycling protocol (95°C for 30s and 58°C for 1 min.), and the final denaturation step at 98°C for 10 min. in accordance with manufacturer instructions (Bio-Rad). The amplification signal was measured using a QX200 Droplet Reader, and data analysis was performed using QuantaSoft software version 1.7.4 (Bio-Rad, USA).

Transcriptome sequencing

Total RNA was extracted from cultured patient-derived primary cells using RNeasy Plus Mini kit. The quality of RNAs was evaluated using an Agilent TapeStation 4200 (Agilent Technologies, USA). Transcriptome sequencing libraries were prepared using the TruSeq Stranded Total RNA LT sample preparation kit to deplete of ribosomal RNA prior to cDNA synthesis. After, indexed adaptors are ligated to cDNA fragments and purified using AMPureXP beads (Beckman Coulter Life Sciences, USA). Sequencing libraries are normalized prior to sequencing using the 150bp paired-end protocol on an Illumina NextSeq2000 instrument.

Transcriptome analyses were conducted using Partek Flow software. Sequence reads were mapped to the human reference genome (hg38) using STAR (v2.7.8). Alignments were filtered to remove low quality reads prior to quantification of gene expression using the Ensembl transcript database. Gene expression was normalized using the median ratio method for DESeq2 analysis. For principal component analysis, systematic differences between patients were removed using general linear modeling. Differential gene expression analysis was performed using DESeq2 including patient and treatment variables. Differentially expressed genes were defined with at least a 2-fold change in expression and false discovery rate (FDR) p-value less than 0.05. Differential gene expression analysis, principal component analysis, heatmap plotting, and hierarchical clustering were performed using Partek Flow software (Illumina, Inc).

Western blotting

Protein was extracted using RIPA buffer (catalog#89900, Thermo Fisher Scientific, USA) with halt protease inhibitor cocktail (catalog#78430, Thermo Fisher Scientific, USA), and phosphatase inhibitor cocktail 2 and 3 (catalog#P5726 and P0044, Sigma Aldrich, USA). Concentration was determined using the Pierce BCA protein assay kit (catalog#23227, Thermo FisherScientific, USA). Lysate samples were denatured in the sample buffer (catalog# BP111NR, Boston Bioproducts, USA) supplemented with beta-mercaptoethanol. Equal amounts of sample (in micrograms) were resolved in 10% polyacrylamide gels (catalog #M00664 and M00666, GenSrcipt, USA) for 1 hour 15 minutes at 120 volts. The wet transfer of resolved proteins was performed for 1 hour at 100 volts at 4°C. Antibody detection was performed using rabbit anti-tERK(1:1000; catalog#4695S, Cell Signaling Technologies, USA), rabbit anti-pERK (1:1000; catalog#4370S, Cell Signaling Technologies, USA), rabbit anti-S6 (1:1000; catalog#4858, Cell Signaling Technologies, USA), and rabbit anti-pS6 (1:1000; catalog#4858, Cell Signaling Technologies, USA) primary antibodies in 1X TBST buffer (10X TBS, catalog#1706435, Biorad, USA, Tween-20, catalog#P9416, Sigma Aldrich, USA) with 5% BSA (calalog#A7906, Sigma Aldrich, USA) overnight at 4°C. After washing three times with 1X TBST buffer, goat anti-rabbit (1:5,000) IRDye secondary antibodies (catalog#926-32211, Licor

Biosciences, USA) were incubated in 5% nonfat dry milk in 1X TBST buffer for 1 hour at room temperature in dark. Following two washes with 1X TBST buffer and one wash with 1X TBS buffer, images were acquired using the Odyssey CLx system (Licor Biosciences, USA). Western quantification was performed using ImageJ software (National Institutes of Health) for human samples and Licor Odessey machine for mouse samples.

Micro-computed tomography (μCT)

Femurs were harvested from 4-month-old control and *Met*$^{\Delta JMD}$ mice and imaged using a Skyscan 1072 X-ray Microtomography (Skyscan, Aartselaar, Belgium, software v1.5) set with voltage 50kV, current of 201μA, exposure time of 650ms, 0.5mm Al filter, average frame of 6, and rotation step of 0.4° per projection. A scout view of each bone was taken, and the sample height was adjusted to ensure the bone was within the field of view. Solid three-dimensional models were reconstructed using NRecon (Skyscan, v1.7.4.6) giving a resolution of 8μm, and the trabecular parameters were measured using methods recommended by Skyscan. Regions of interest were analyzed using CTan software (v1.20.3.0). The trabecular parameters were calculated on 200 slices of trabecular bone from 50 slices below the growth plate with a threshold of 90-255 grayscale values. Measurements were calculated using the American Society of Bone and Mineral Research nomenclature (43). Likewise, the cortical parameters were calculated on 100 slices from mid-diaphysis with a threshold of 138-255 grayscale values.

Biomechanical testing

Hydrated, intact femurs were loaded to failure in three-point bending at a rate of 3 mm/min using a material testing instrument (Instron Dynamight 8841, Instron inc., Norwood, MA) to assess the biomechanical properties of the cortical bone. Each femur was centered on the three-point bending fixture with the medial side facing forward and the anterior side facing down (i.e., anterior in tension). The span between the 2 supports was 8 mm for all tests. The linear variable differential transformer (LVDT) attached to the linear actuator and a 100 N load cell mounted in line with the actuator recorded the force vs. displacement data at a sampling rate of 50 Hz. As described previously (44, 45), this data was analyzed to determine stiffness.

Statistical analysis

Except for transcriptome analyses, all data are represented by mean and standard error of the mean (SEM) from multiple replicates from independent experiments performed on different days. Most data were normalized using a log transformation, and statistical tests were performed using GraphPad Prism. Sample sizes were not pre-determined and mice were randomly assigned to experiments. Sex-matched littermate controls were used for all experiments. A P value less than 0.05 was considered significant.

Study approvals

Patient-derived primary cells were provided by the Scottish Rite for Children Biorepository following written informed consent approved by the Institutional Review Board at UT Southwestern Medical Center (STU#092011-034) for the collection and use of discard surgical waste, including excess graft and resected pseudarthrosis tissue. Off-label compassionate use treatment with mirdametinib was administered following FDA and UT Southwestern Medical Center Institutional Review Board regulatory approval and parental informed consent (IND#175099). Mirdametinib was provided by SpringWorks Therapeutics, Inc. (Stamford, Connecticut) as part of its compassionate use program.

All rodent procedures were approved by the Institutional Animal Care and Use Committee at UT Southwestern Medical Center (APN#2016-101455).

Data availability

Supporting data values are provided in the Supporting Data Values file. RNA-seq data are available from the NCBI's Gene Expression Omnibus database (GEO GSE305253).

AUTHOR CONTRIBUTIONS

A.K., C.A.W., and J.J.R. designed the research study. A.K., K.D., N.P., I.O., R.C., S.U., G.J.J., C.R.F., R.H., J.R., M.N., D.P., and L.J.K. conducted experiments. A.K., N.P., I.O., S.U., J.S.N., G.J.J., C.R.F., and J.J.R. analyzed data. S.J.C. provided reagents. A.K. and J.J.R. wrote the manuscript. All authors reviewed and edited the manuscript.

FUNDING SUPPORT

This work is the result of NIH funding, in whole or in part, and is subject to the NIH Public Access Policy. Through acceptance of this federal funding, the NIH has been given a right to make the work publicly available in PubMed Central.

- Pediatric Orthopaedic Society of North America award #822001 (to JJR).
- Department of Defense award W81XWH-22-1-0576 (to JJR).
- Scottish Rite for Children (to JJR).
- NIH grant ZIA HD009024 (to CRF).

ACKNOWLEDGEMENTS

The authors wish to thank the efforts of the UT Southwestern Next-Generation Sequencing core facility, staff of the UT Southwestern Animal Resource Center, and the orthopaedic staff at Scottish Rite for Children. SpringWorks Therapeutics, Inc was offered the opportunity to review and provide comment on the scientific accuracy of the manuscript. Changes resulting from any comments provided by SpringWorks were made solely at the discretion of the authors.

FIGURE LEGENDS

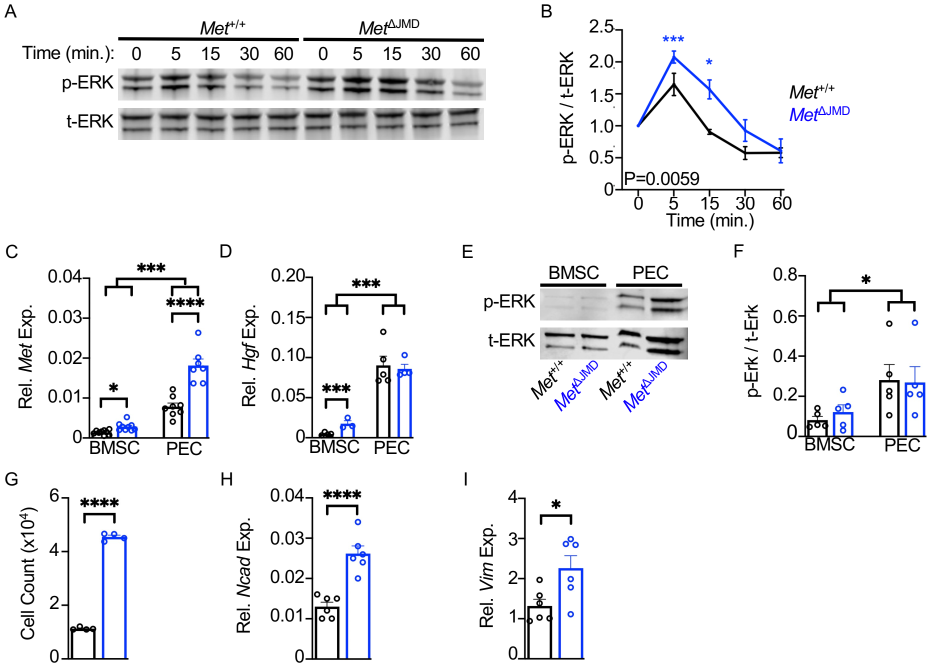

Figure 1. Characterization of $\mathit{Met}^{\Delta\mathrm{JMD}}$ osteoprogenitor cells. **(A and B)** Representative western blot time course (A) and quantification (B) of ERK activation following HGF stimulation of BMSCs from control (black; n=3) or $\mathit{Met}^{\Delta\mathrm{JMD}}$ (blue; n=5) mice. Statistical analysis was conducted by 2-way ANOVA with Dunett multiple test correction including only 5 and 15 min. timepoints. **(C** and **D)** Relative expression of *Met* (C) and *Hgf* (D) in BMSCs and PECs from control (n=8-9) and $\mathit{Met}^{\Delta\mathrm{JMD}}$ (n=7-9) mice. Statistically significant differences were determined by 2-way ANOVA with Sidak multiple test correction. **(E** and **F)** Representative western blot (E) and quantification (F) of ERK pathway activation of serum-starved BMSCs and PECs from control (n=5) and $\mathit{Met}^{\Delta\mathrm{JMD}}$ (n=5) mice. Statistically significant differences were determined by 2-way ANOVA with Sidak multiple test correction. **(G)** Cell count quantification of PECs from control (n=4) and $\mathit{Met}^{\Delta\mathrm{JMD}}$ (n=4) mice. Statistically significant differences were determined by T-test. **(H** and **I)** Relative expression of mesenchymal adhesion genes *Ncad* (H) and *Vim* (I) in PECs from control (n=6) and $\mathit{Met}^{\Delta\mathrm{JMD}}$ (n=6) mice. Statistically significant differences were determined by T-test. RT-qPCR from cultured cells and other quantification data are presented as mean ± SEM. *, $p<0.05$; **, $p<0.01$; ***, $p<0.001$; ****, $p<0.0001$.

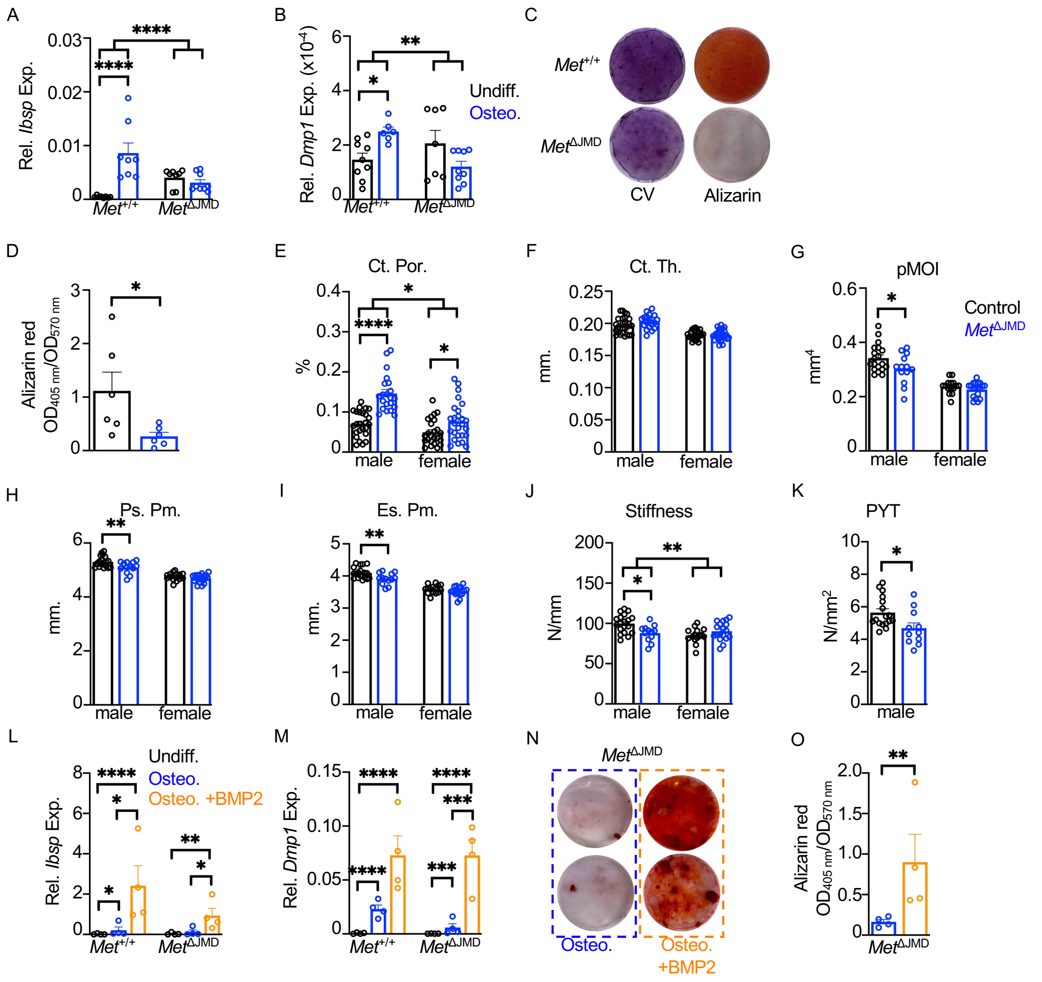

Figure 2. Impaired osteogenic differentiation of PECs from *Met*$^{\Delta JMD}$ mice. **(A and B)** Relative expression of the osteogenic genes *Ibsp* (A) and *Dmp1* (B) in control (n=4-9) and *Met*$^{\Delta JMD}$ (n=4-9) PECs prior to (undifferentiated, black) and following osteogenic differentiation (Osteo., blue). Statistically significant differences were determined by 2-way ANOVA with Sidak multiple test correction. **(C and D)** Representative alizarin red and Crystal violet (CV) staining (C) and quantification (D) following osteogenic differentiation of control (Met$^{+/+}$; n=6) and *Met*$^{\Delta JMD}$ (n=6) PECs. Statistically significant differences were determined by T-test. **(E-J)** Quantification of cortical porosity (E; Ct. Por.), cortical thickness (F; Ct. Th.), polar Moment of Inertia (G; pMOI), periosteal perimeter (H; Pl. Pm), endosteal perimeter (I; Es. Pm.), and stiffness (J) of femurs from 4-month-old male and female control (black; n=15-49) and *Met*$^{\Delta JMD}$ (blue; n=13-47) male and female mice. Statistically significant differences were determined by 2-way ANOVA with Sidak multiple test correction. **(K)** Quantification of post-yield toughness (PYT) of femurs from 4-month-old male control (n=17) and *Met*$^{\Delta JMD}$ (n=11) mice. Statistically significant differences were determined by T-test. **(L and M)** Relative expression of osteogenic genes *Ibsp* (L) and *Dmp1* (M) prior to differentiation (Undiff., black) or following standard osteogenic differentiation (Osteo., blue) or osteogenic differentiation with BMP2 (Osteo.+BMP2, orange) in control (n=5) and *Met*$^{\Delta JMD}$ (n=5-6) PECs. Statistically significant differences were determined by 2-way ANOVA with Tukey multiple test correction. **(N and O)** Representative alizarin red staining (N) and quantification (O) following osteogenic differentiation of *Met*$^{\Delta JMD}$ PECs. Statistically significant differences were determined by T-test (n=4 per group). RT-qPCR from

cultured cells and other quantification data are presented as mean ± SEM. *, $p<0.05$; **, $p<0.01$; ****, $p<0.0001$.

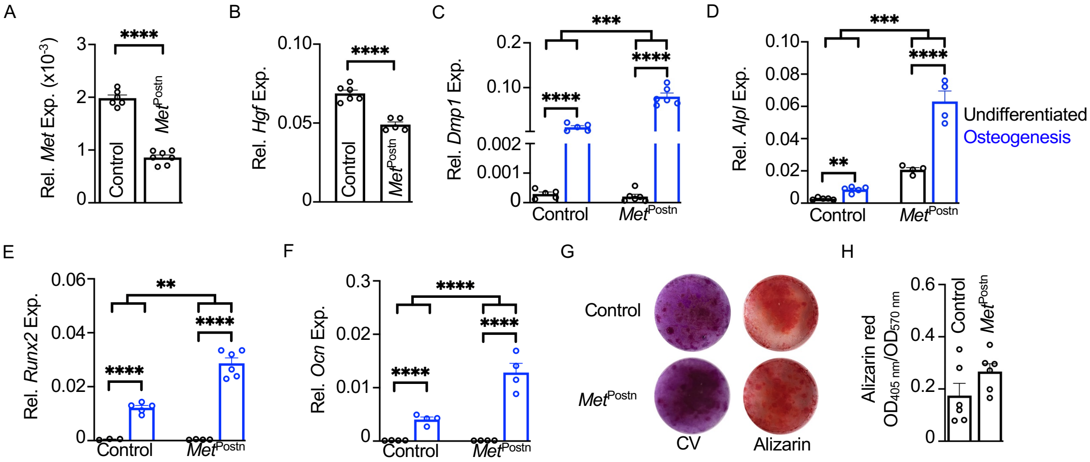

Figure 3. Osteogenic differentiation of PECs from *Met*$^{\text{Postn}}$ mice. **(A and B)** Relative expression of *Met* (A) and *Hgf* (B) in PECs from control (n=6) and *Met*$^{\text{Postn}}$ (n=7) mice. Statistically significant differences were determined by T-test. **(C-F)** Relative expression of the osteogenic marker genes *Dmp1* (C), *Alpl* (D), *Runx2* (E), and *Ocn* (F) prior to (Undiff., black) and following osteogenic differentiation (Osteogenesis, blue) of PECs from control (n=3) and *Met*$^{\text{Postn}}$ (n=4-6) mice. Statistically significant differences were determined by 2-way ANOVA with Sidak multiple test correction. **(G and H)** Representative Crystal violet (CV) and Alizarin red staining (G) and quantification (H) of PEC from control and *Met*$^{\text{Postn}}$ mice following osteogenic differentiation (n=6 per group). Statistically significant differences were determined by T-test. RT-qPCR from cultured cells and other quantification data are presented as mean ± SEM. **, p<0.01; ***, p<0.001; ****, p<0.0001.

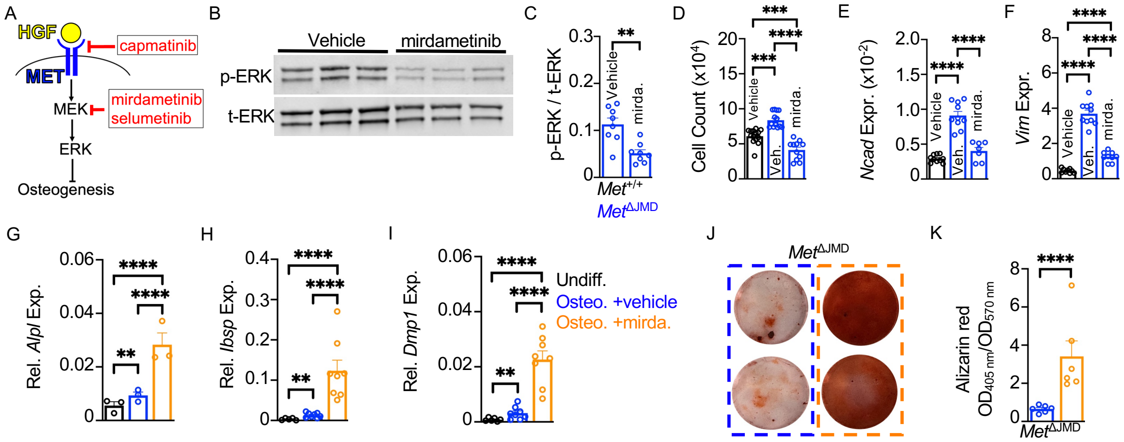

Figure 4. MEK inhibition rescues osteogenic differentiation of *Met*$^{\Delta\text{JMD}}$ PECs. **(A)** Schematic of the MET receptor (blue) bound by HGF (yellow) to activate the downstream MEK/ERK signaling cascade to regulate osteogenic differentiation of skeletal progenitor cells. Pharmacologic inhibitors of MET (capmatinib) and MEK (mirdametinib, selumetinib) are shown in red. **(B** and **C)** Representative western blot (B) and quantification (C) of ERK pathway activation in *Met*$^{\Delta\text{JMD}}$ PECs treated with vehicle (n=8) or mirdametinib (mirda.; n=8). Statistically significant differences were determined by T-test. **(D)** Cell count quantification of PECs from control (n=14) and *Met*$^{\Delta\text{JMD}}$ (n=14) mice. Statistically significant differences were determined by 1-way ANOVA with Tukey multiple test correction. **(E** and **F)** Relative expression of cell adhesion genes *Ncad* (E) and *Vim* (F) in control (*Met*$^{+/+}$; n=9-10) and *Met*$^{\Delta\text{JMD}}$ (n=7-10) PECs treated with vehicle (Veh.) or mirdametinib. Statistically significant differences were determined by 1-way ANOVA with Tukey multiple test correction. **(G-I)** Relative expression of the osteogenic genes *Alpl* (G), *Ibsp* (H) and *Dmp1* (I) in *Met*$^{\Delta\text{JMD}}$ PECs prior to (Undiff., black) or following osteogenic differentiation in the presence of vehicle (Osteo.+vehicle, blue) or mirdametinib (Osteo.+mirda., orange) (n=3-8 per group). Statistically significant differences were determined by 1-way ANOVA with Tukey multiple test correction. **(J** and **K)** Representative Alizarin red staining (J) and quantification (K) of *Met*$^{\Delta\text{JMD}}$ PECs following osteogenic differentiation in the presence of vehicle (blue, n=6) or mirdametinib (orange, n=6). Statistically significant differences were determined by T-test. RT-qPCR from cultured cells and other quantification data are presented as mean ± SEM. **, $p<0.01$; ***, $p<0.001$; ****, $p<0.0001$.

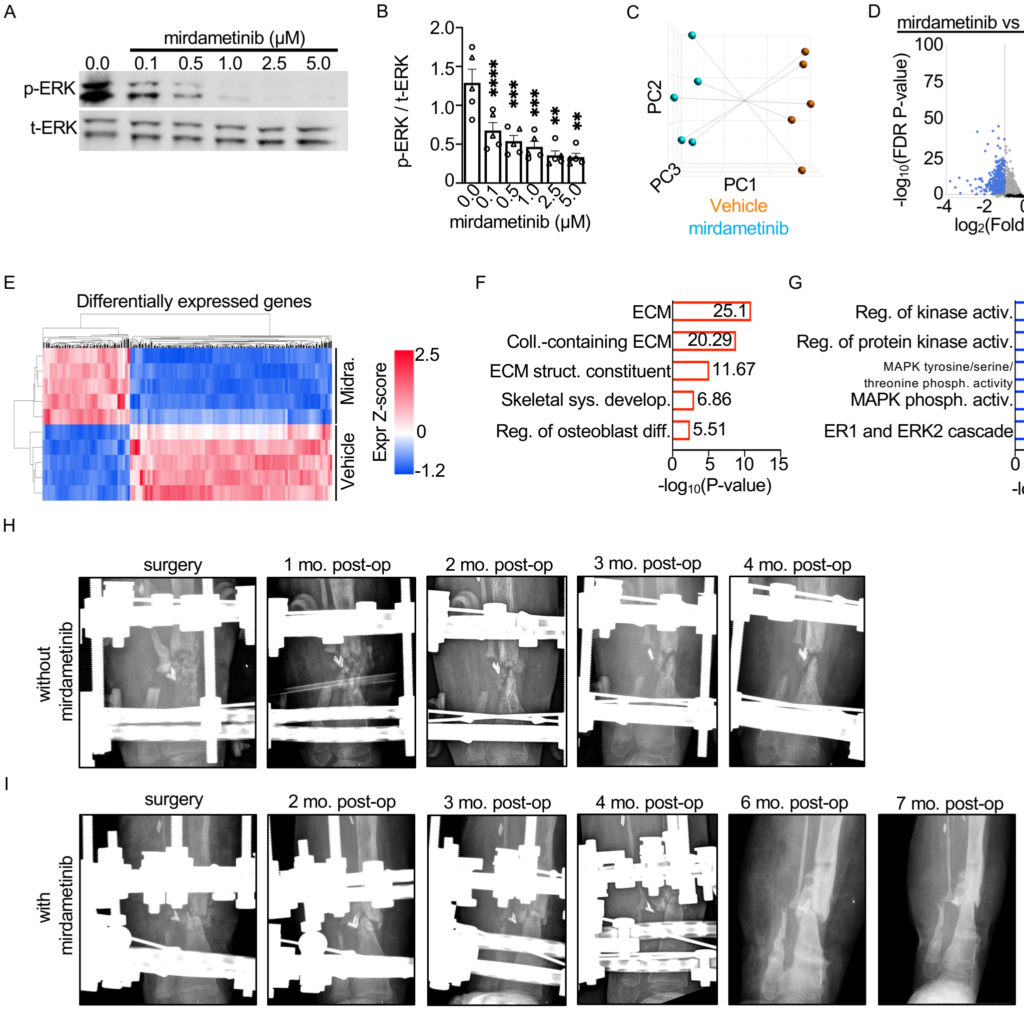

Figure 5. Mirdametinib improves pseudarthrosis healing in a OFD patient. **(A and B)** Representative western blot (A) and quantification (B) demonstrating dose-dependent reduction in ERK pathway activation in OFD patient pseudarthrosis-derived primary cells (n=5) treated with mirdametinib. Triangles indicate samples with somatic *MET* mutations. Circles indicate samples without detectable *MET* mutations. Quantification data are presented as mean ± SEM. with statistically significant differences determined by 1-way ANOVA with Dunnett multiple test correction. **(C)** Principal component analysis of OFD patient pseudarthrosis-derived primary cells treated with vehicle or mirdametinib (n=5). **(D and E)** Volcano plot (D) and heatmap (E) of genes differentially expressed between mirdametinib- and vehicle-treated OFD patient pseudarthrosis-derived primary cells. **(F and G)** Gene ontology analysis of differentially expressed genes with increased (F) and decreased (G) expression following mirdametinib treatment. **(H and I)** Longitudinal post-operative radiographs of an OFD patient pseudarthrosis treated without mirdametinib (H) and with mirdametinib (I). **, $p<0.01$; ***, $p<0.001$

Supplemental Figure 1

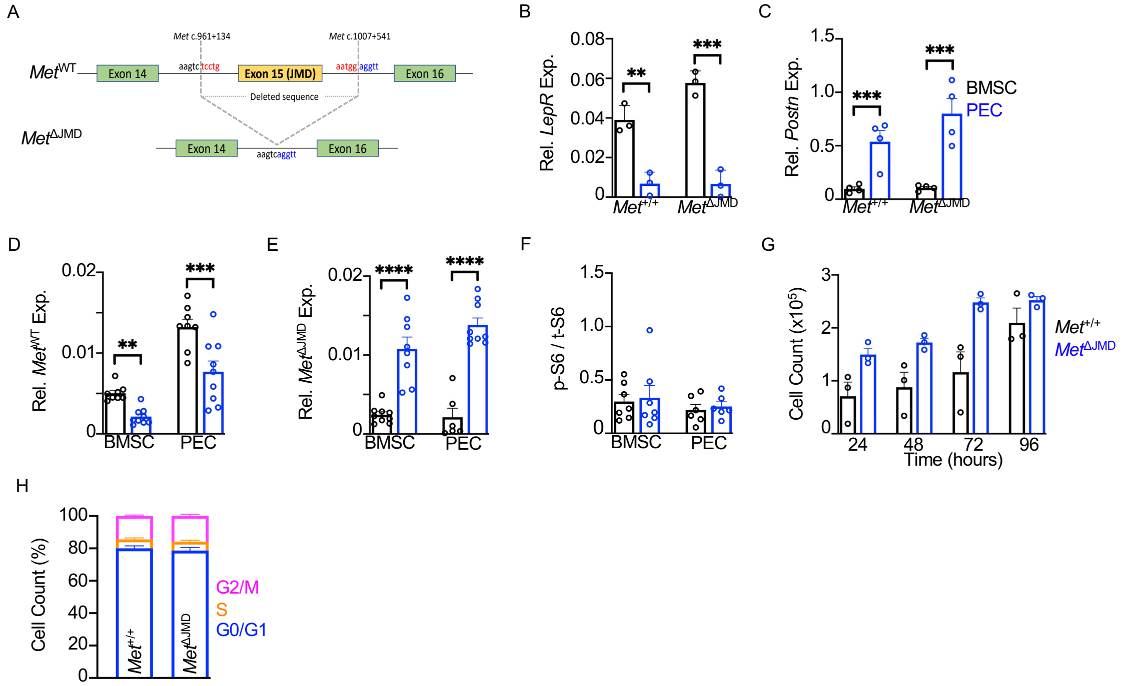

Supplemental Figure 1. Confirmation of skeletal progenitor cell populations. **(A)** Schematic of the *Met* locus indicating the location of the exon 15 deletion in *Met*$^{\Delta JMD}$ mice. **(**B and **C)** Relative expression of the BMSC marker gene *LepR* (B) and the PEC marker gene *Postn* (C) in control (*Met*$^{+/+}$; n=3-4) and *Met*$^{\Delta JMD}$ (n=3-4) BMSCs (black) and PECs (blue). Statistically significant differences were determined by 2-way ANOVA with Sidak multiple test correction. **(D** and **E)** Allele-specific expression of wild-type (D) and mutant (E) *Met* alleles in control (*Met*$^{+/+}$; n=6-9) and *Met*$^{\Delta JMD}$ (n=8-9) BMSCs and PECs. Statistically significant differences were determined by 2-way ANOVA with Sidak multiple test correction. **(F)** Western blot quantification of S6 activation in serum-starved BMSCs and PECs from control (n=7) and *Met*$^{\Delta JMD}$ (n=6) mice. **(G)** Time-course cell count quantification of PECs from control (n=3) and *Met*$^{\Delta JMD}$ (n=3) mice. Statistically significant differences were determined by 2-way ANOVA with Sidak multiple test correction. **(H)** Quantification of cell cycle stage by flow cytometric analysis of PECs from control and *Met*$^{\Delta JMD}$ mice (n=3 per group). RT-qPCR from cultured cells and other quantification data are presented as mean ± SEM. **, p<0.01; ***, p<0.001; ****, p<0.0001.

Supplemental Figure 2

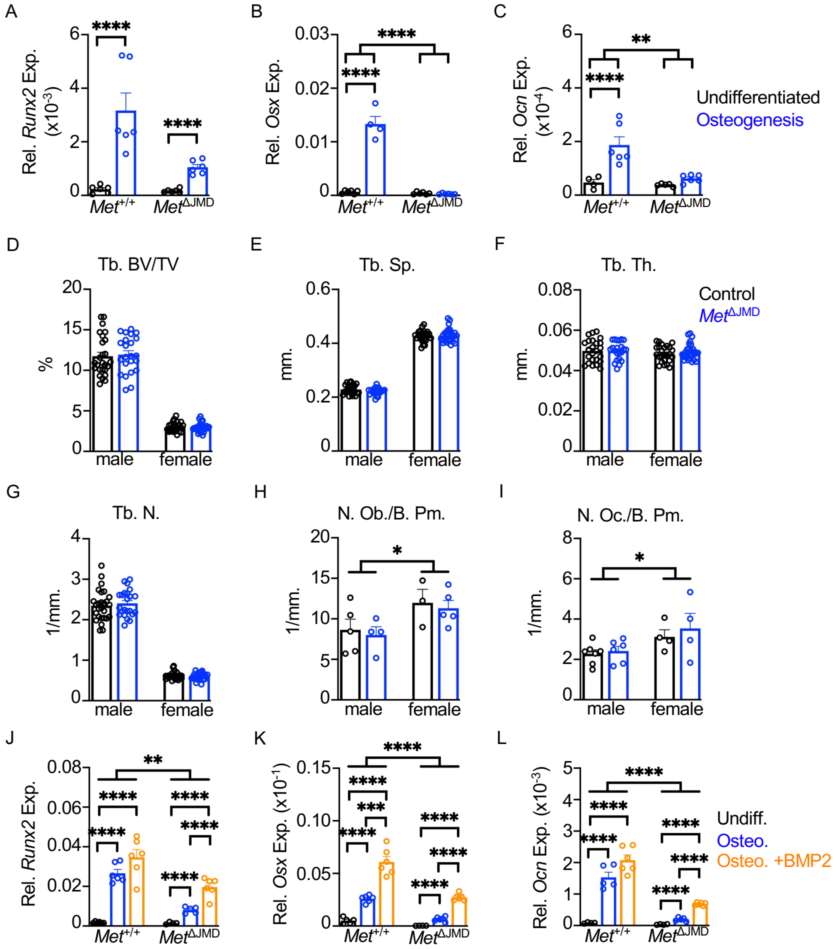

Supplemental Figure 2. Microstructure analysis of adult *Met*$^{\Delta\text{JMD}}$ mice. **(A-C)** Relative expression of the osteogenic genes *Runx2* (A), *Osx* (B), and *Ocn* (C) in control (n=4-6) and *Met*$^{\Delta\text{JMD}}$ (n=6) PECs prior to (undifferentiated, black) and following osteogenic differentiation (Osteogenesis, blue). Statistically significant differences were determined by 2-way ANOVA with Sidak multiple test correction. **(D-G)** Distal femur trabecular bone volume/tissue volume (D; Tb. BVTV), trabecular spacing (E; Tb. Sp.), trabecular thickness (F; Tb. Th.), and trabecular number (G; Tb. N.) in control (black; n=49-52) and *Met*$^{\Delta\text{JMD}}$ (blue; n=50-51) male and female mice. Statistically significant differences were determined by 2-way ANOVA with Sidak multiple test correction. **(H-I)** Osteoblast number per trabecular bone perimeter (H; N. Ob./B. Pm.) and osteoclast number per trabecular bone perimeter (I; N. Oc./B. Pm.) in control (black; n=3-7) and *Met*$^{\Delta\text{JMD}}$ (blue; n=4-6) male and female mice. Statistically significant differences were determined by 2-way ANOVA with Sidak multiple test correction. **(J-L)** Relative expression of the osteogenic genes *Runx2* (J), *Osx* (K), and *Ocn* (L) in control (n=4-6) and *Met*$^{\Delta\text{JMD}}$ (n=4-6) PECs prior to (undifferentiated, black) or following standard osteogenic differentiation (Osteo., blue) or osteogenic differentiation with BMP2 (Osteo.+BMP2, orange). Statistically significant differences were determined by 2-way ANOVA with Tukey multiple test correction. RT-qPCR from cultured cells and other quantification data are presented as mean ± SEM. *, $p<0.05$; **, $p<0.01$; ***, $p<0.001$; ****, $p<0.0001$.

Supplemental Figure 3

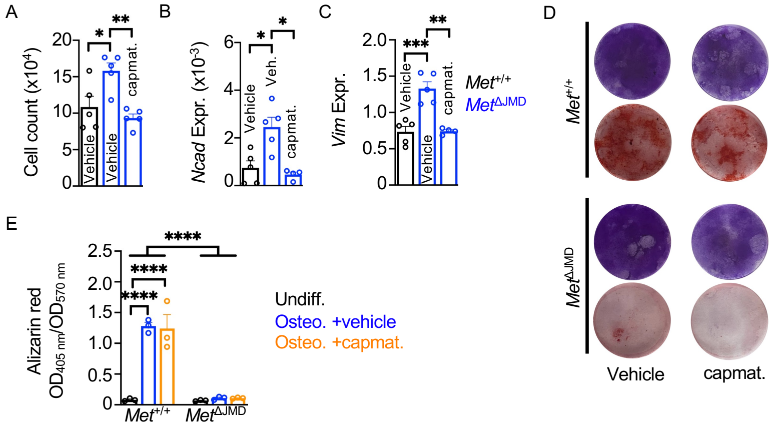

Supplemental Figure 3. Response of *Met*$^{\Delta JMD}$ PECs to capmatinib treatment. **(A)** Quantification of cell adhesion in control (*Met*$^{+/+}$) or *Met*$^{\Delta JMD}$ (blue) PECs treated with vehicle (Veh.) or capmatinib (capmat.) (n=5 per group). Statistically significant differences were determined by 1-way ANOVA with Tukey multiple test correction. **(B and C)** Relative expression of cell adhesion genes *Ncad* (B) and *Vim* (C) in control or *Met*$^{\Delta JMD}$ PECs treated with vehicle or capmatinib (n=4-5 per group). Statistically significant differences were determined by 1-way ANOVA with Tukey multiple test correction. **(D)** Representative Alizarin red and Crystal Violoet (CV) staining following osteogenic differentiation of control and *Met*$^{\Delta JMD}$ PECs treated with vehicle or capmatinib. **(E)** Quantification of alizarin staining of control (*Met*$^{+/+}$) and *Met*$^{\Delta JMD}$ PECs prior to (Undiff.) or following osteogenic differentiation (Osteo.) with vehicle or capmatinib (capmat.) (n=3 per group). Statistically significant differences were determined by 2-way ANOVA with Tukey multiple test correction. RT-qPCR from cultured cells and other quantification data are presented as mean ± SEM. *, $p<0.05$; **, $p<0.01$; ***, $p<0.001$; ****, $p<0.0001$.

Supplemental Figure 4

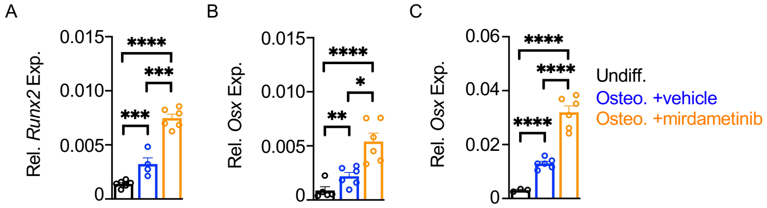

Supplemental Figure 4. Response of *Met*$^{\Delta \mathrm{JMD}}$ PECs to mirdametinib treatment. **(A-C)** Relative expression of the osteogenic genes *Runx2* (A), *Osx* (B), and *Ocn* (C) in *Met*$^{\Delta \mathrm{JMD}}$ PECs prior to (Undiff., black) or following osteogenic differentiation in the presence of vehicle (Osteo.+vehicle, blue) or mirdametinib (Osteo.+ mirdametinib, orange) (n=3-6 per group). Statistically significant differences were determined by 1-way ANOVA with Tukey multiple test correction. RT-qPCR from cultured cells and other quantification data are presented as mean ± SEM. *, $p<0.05$; **, $p<0.01$; ***, $p<0.001$; ****, $p<0.0001$.

Supplemental Figure 5

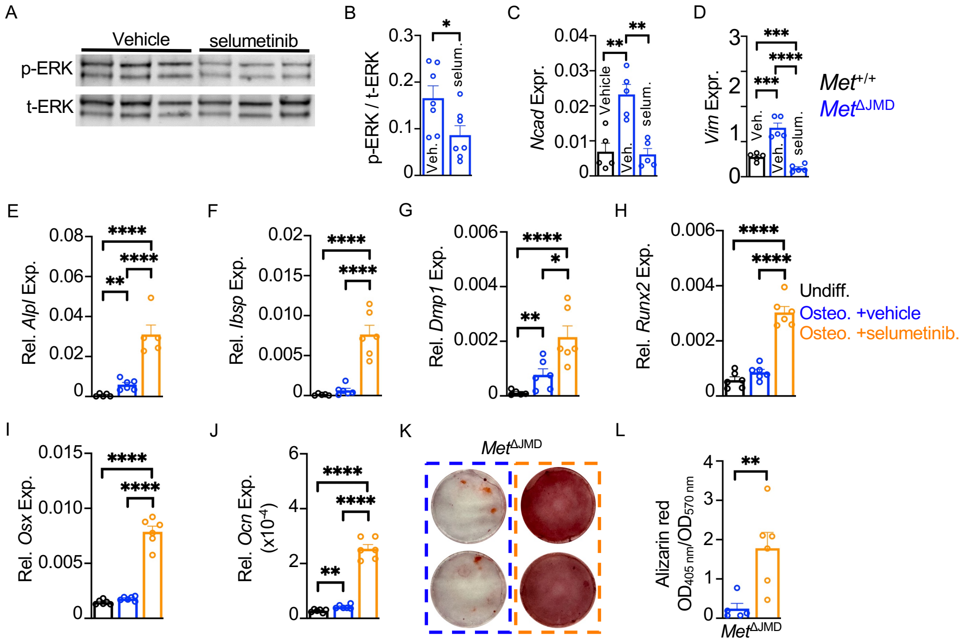

Supplemental Figure 5. Response of $Met^{\Delta JMD}$ PECs to selumetinib treatment. **(A and B)** Representative western blot (A) and quantification (B) demonstrating reduced ERK pathway activation with selumetinib treatment (n=7 per group). Statistically significant differences were determined by T-test. **(C and D)** Relative expression of cell adhesion genes *Ncad* (C) and *Vim* (D) in control ($Met^{+/+}$) or $Met^{\Delta JMD}$ PECs treated with vehicle or selumetinib (n=5 per group). Statistically significant differences were determined by 1-way ANOVA with Tukey multiple test correction. **(E-J)** Relative expression of the osteogenic genes *Alpl* (E), *Ibsp* (F), *Dmp1* (G), *Runx2* (H), *Osx* (I), and *Ocn* (J) in $Met^{\Delta JMD}$ PECs prior to (Undiff., black) or following osteogenic differentiation in the presence of vehicle (Osteo.+vehicle, blue) or selumetinib (Osteo.+selumetinib, orange) (n=5-6 per group). Statistically significant differences were determined by 1-way ANOVA with Tukey multiple test correction. **(K)** Representative Alizarin red staining following osteogenic differentiation of $Met^{\Delta JMD}$ PECs treated with vehicle (blue) or selumetinib (orange). **(L)** Quantification of alizarin staining $Met^{\Delta JMD}$ PECs following osteogenic differentiation with vehicle (blue; n=5) or selumetinib (orange; n=6). Statistically significant differences were determined by T-test. RT-qPCR from cultured cells and other quantification data are presented as mean ± SEM. *, $p<0.05$; **, $p<0.01$; ***, $p<0.001$; ****, $p<0.0001$.

Supplemental Figure 6

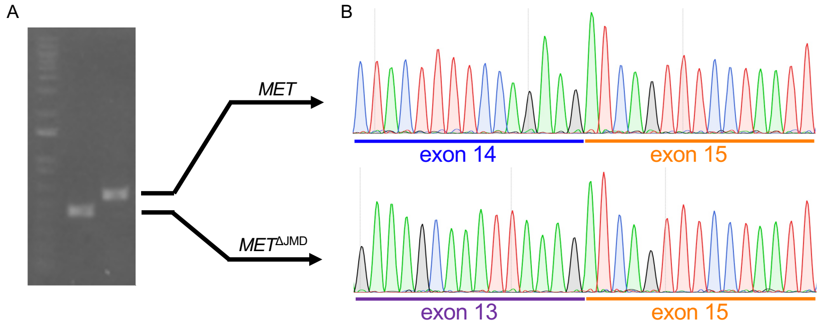

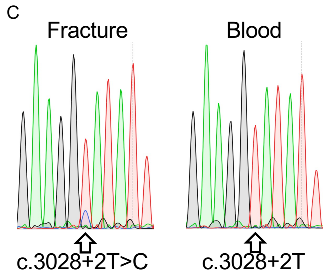

D

	Replicate 1			Replicate 2		
	Mutant allele (copies/μL)	Ref. allele (copies/μl)	VAF (%)	Mutant allele (copies/μL)	Ref. allele (copies/μl)	VAF (%)
Lesion	266	1,474	18.1	229	1,131	20.2
Blood	0	2,883	0	0	2,768	0

Supplemental Figure 6. Somatic *MET* mutation in human sporadic OFD. **(A** and **B)** RT-PCR (A) and Sanger sequencing (B) confirmation of *MET*$^{\Delta JMD}$ expression in clonal amplicons from pseudarthrosis-derived primary cells from an OFD patient. **(C** and **D)** Sanger sequence confirmation (C) and droplet digital PCR quantification (D) of the somatic splice-site mutation c.3028+2T>C using DNA from cultured pseudarthrosis-derived primary cells or patient-matched blood from an OFD patient.

Supplemental Figure 7

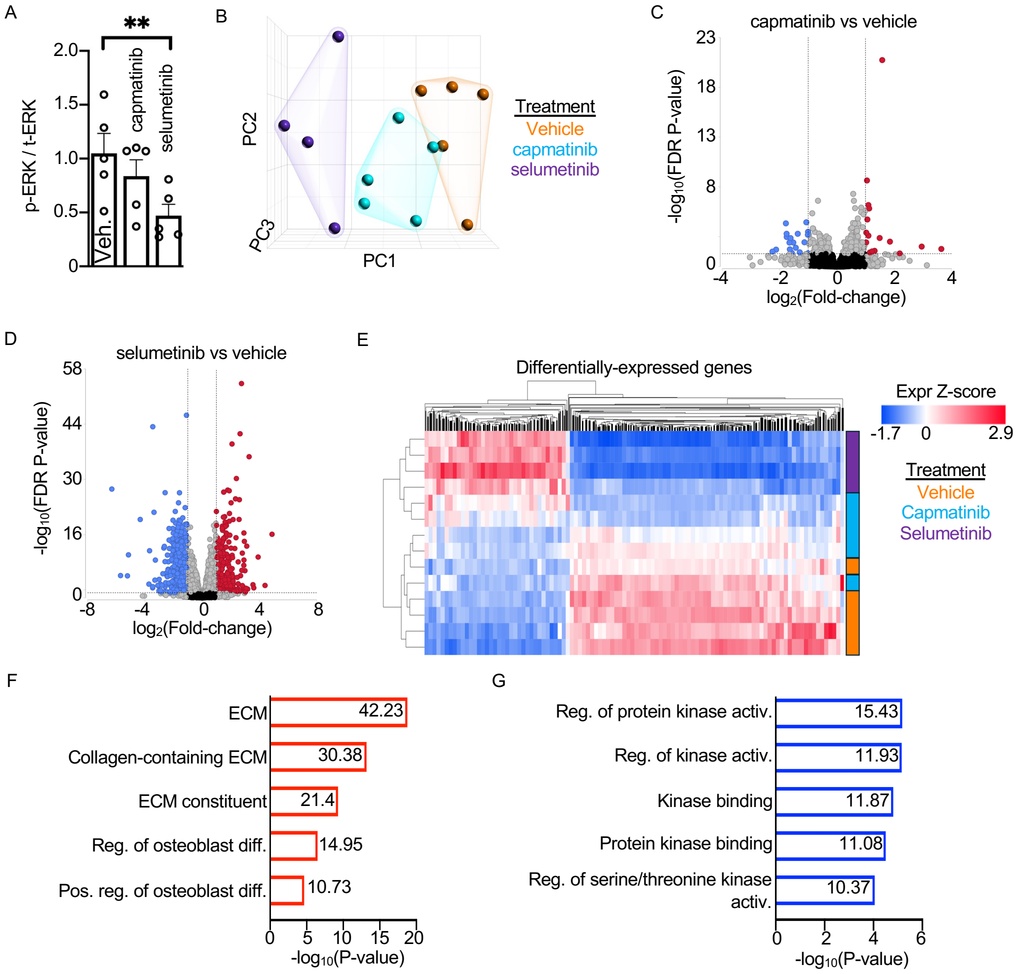

Supplemental Figure 7. Molecular characterization of patient OFD-derived primary cells. **(A)** Quantification of ERK pathway activation in OFD lesion-derived primary cells treated with vehicle (Veh.), capmatinib, or selumetinib (n=5 per group). Quantification is presented as mean ± SEM. with significant differences determined by 1-way ANOVA with Dunnett multiple test correction. **(B)** Principal component analysis from RNA-seq analysis of OFD pseudarthrosis-derived primary cells treated with vehicle (orange), capmatinib (blue), or selumetinib (purple). **(C** and **D)** Volcano plot showing differentially expressed genes between capmatinib (C) or selumetinib (D) treated samples compared to vehicle. **(E)** Heatmap of genes differentially expressed following selumetinib treatment across all samples treated with vehicle (orange), capmatinib (blue), or selumetinib (purple). **(F** and **G)** Gene ontology analysis of differentially expressed genes with increased (F) or decreased (G) expression following selumetinib treatment. Enrichment values for each category are indicated. **, p<0.01.

REFERENCES

1. Park YK, Unni KK, McLeod RA, and Pritchard DJ. Osteofibrous dysplasia: clinicopathologic study of 80 cases. *Hum Pathol.* 1993;24(12):1339-47.
2. Sunkara UK, Sponseller PD, Hadley Miller N, and McCarthy EF. Bilateral osteofibrous dysplasia: a report of two cases and review of the literature. *Iowa Orthop J.* 1997;17:47-52.
3. Karol LA, Brown DS, Wise CA, and Waldron M. Familial osteofibrous dysplasia. A case series. *J Bone Joint Surg Am.* 2005;87(10):2297-307.
4. Gray MJ, Kannu P, Sharma S, Neyt C, Zhang D, Paria N, et al. Mutations Preventing Regulated Exon Skipping in MET Cause Osteofibrous Dysplasia. *Am J Hum Genet.* 2015;97(6):837-47.
5. Beals RK, and Fraser W. Familial congenital bowing of the tibia with pseudarthrosis and pectus excavatum: report of a kindred. *J Bone Joint Surg Am.* 1976;58(4):545-8.
6. Herring JA ed. *Tachdjian's Pediatric Orthopaedics*. Philadelphia: WB Saunders; 2021.
7. Owusu BY, Galemmo R, Janetka J, and Klampfer L. Hepatocyte Growth Factor, a Key Tumor-Promoting Factor in the Tumor Microenvironment. *Cancers (Basel).* 2017;9(4).
8. Van Der Steen N, Giovannetti E, Pauwels P, Peters GJ, Hong DS, Cappuzzo F, et al. cMET Exon 14 Skipping: From the Structure to the Clinic. *Journal of thoracic oncology : official publication of the International Association for the Study of Lung Cancer.* 2016;11(9):1423-32.
9. Lefebvre J, Ancot F, Leroy C, Muharram G, Lemiere A, and Tulasne D. Met degradation: more than one stone to shoot a receptor down. *FASEB J.* 2012;26(4):1387-99.

10. Lu X, Peled N, Greer J, Wu W, Choi P, Berger AH, et al. MET Exon 14 Mutation Encodes an Actionable Therapeutic Target in Lung Adenocarcinoma. *Cancer Res.* 2017;77(16):4498-505.

11. Furlan A, Kherrouche Z, Montagne R, Copin MC, and Tulasne D. Thirty years of research on met receptor to move a biomarker from bench to bedside. *Cancer Res.* 2014;74(23):6737-44.

12. Pilotto S, Gkountakos A, Carbognin L, Scarpa A, Tortora G, and Bria E. MET exon 14 juxtamembrane splicing mutations: clinical and therapeutical perspectives for cancer therapy. *Ann Transl Med.* 2017;5(1):2.

13. Weinstein IB. Cancer. Addiction to oncogenes--the Achilles heal of cancer. *Science.* 2002;297(5578):63-4.

14. Wolf J, Seto T, Han JY, Reguart N, Garon EB, Groen HJM, et al. Capmatinib in MET Exon 14-Mutated or MET-Amplified Non-Small-Cell Lung Cancer. *N Engl J Med.* 2020;383(10):944-57.

15. Paik PK, Felip E, Veillon R, Sakai H, Cortot AB, Garassino MC, et al. Tepotinib in Non-Small-Cell Lung Cancer with MET Exon 14 Skipping Mutations. *N Engl J Med.* 2020;383(10):931-43.

16. Graveel C, Su Y, Koeman J, Wang LM, Tessarollo L, Fiscella M, et al. Activating Met mutations produce unique tumor profiles in mice with selective duplication of the mutant allele. *Proc Natl Acad Sci U S A.* 2004;101(49):17198-203.

17. Kong-Beltran M, Seshagiri S, Zha J, Zhu W, Bhawe K, Mendoza N, et al. Somatic mutations lead to an oncogenic deletion of met in lung cancer. *Cancer Res.* 2006;66(1):283-9.

18. Sylvester PW. Targeting met mediated epithelial-mesenchymal transition in the treatment of breast cancer. *Clin Transl Med.* 2014;3(1):30.

19. Lu W, and Kang Y. Epithelial-Mesenchymal Plasticity in Cancer Progression and Metastasis. *Dev Cell.* 2019;49(3):361-74.

20. Sim WJ, Iyengar PV, Lama D, Lui SKL, Ng HC, Haviv-Shapira L, et al. c-Met activation leads to the establishment of a TGFbeta-receptor regulatory network in bladder cancer progression. *Nat Commun.* 2019;10(1):4349.

21. Wood GE, Hockings H, Hilton DM, and Kermorgant S. The role of MET in chemotherapy resistance. *Oncogene.* 2021;40(11):1927-41.

22. de la Croix Ndong J, Makowski AJ, Uppuganti S, Vignaux G, Ono K, Perrien DS, et al. Asfotase-alpha improves bone growth, mineralization and strength in mouse models of neurofibromatosis type-1. *Nat Med.* 2014;20(8):904-10.

23. Kolanczyk M, Kossler N, Kuhnisch J, Lavitas L, Stricker S, Wilkening U, et al. Multiple roles for neurofibromin in skeletal development and growth. *Hum Mol Genet.* 2007;16(8):874-86.

24. Papadopoulou A, and Bountouvi E. Skeletal defects and bone metabolism in Noonan, Costello and cardio-facio-cutaneous syndromes. *Front Endocrinol (Lausanne).* 2023;14:1231828.

25. Duplaquet L, Kherrouche Z, Baldacci S, Jamme P, Cortot AB, Copin MC, et al. The multiple paths towards MET receptor addiction in cancer. *Oncogene.* 2018;37(24):3200-15.

26. LoRusso PM, Krishnamurthi SS, Rinehart JJ, Nabell LM, Malburg L, Chapman PB, et al. Phase I pharmacokinetic and pharmacodynamic study of the oral MAPK/ERK kinase

inhibitor PD-0325901 in patients with advanced cancers. *Clin Cancer Res.* 2010;16(6):1924-37.

27. Moertel CL, Hirbe AC, Shuhaiber HH, Bielamowicz K, Sidhu A, Viskochil D, et al. ReNeu: A Pivotal, Phase IIb Trial of Mirdametinib in Adults and Children With Symptomatic Neurofibromatosis Type 1-Associated Plexiform Neurofibroma. *J Clin Oncol.* 2025;43(6):716-29.

28. Gross AM, Wolters PL, Dombi E, Baldwin A, Whitcomb P, Fisher MJ, et al. Selumetinib in Children with Inoperable Plexiform Neurofibromas. *N Engl J Med.* 2020;382(15):1430-42.

29. Rizvi NA, Hellmann MD, Snyder A, Kvistborg P, Makarov V, Havel JJ, et al. Cancer immunology. Mutational landscape determines sensitivity to PD-1 blockade in non-small cell lung cancer. *Science.* 2015;348(6230):124-8.

30. Zehir A, Benayed R, Shah RH, Syed A, Middha S, Kim HR, et al. Mutational landscape of metastatic cancer revealed from prospective clinical sequencing of 10,000 patients. *Nat Med.* 2017;23(6):703-13.

31. Paria N, Oxendine I, Podeszwa D, Wassell M, Cornelia R, Wise CA, et al. Molecular Evidence Supporting MEK Inhibitor Therapy in NF1 Pseudarthrosis. *J Bone Joint Surg Am.* 2025;107(10):1098-106.

32. Campanacci M, and Laus M. Osteofibrous dysplasia of the tibia and fibula. *J Bone Joint Surg Am.* 1981;63(3):367-75.

33. Paria N, Cho TJ, Choi IH, Kamiya N, Kayembe K, Mao R, et al. Neurofibromin deficiency-associated transcriptional dysregulation suggests a novel therapy for tibial pseudoarthrosis in NF1. *J Bone Miner Res.* 2014;29(12):2636-42.

34. Stevenson DA, Zhou H, Ashrafi S, Messiaen LM, Carey JC, D'Astous JL, et al. Double inactivation of NF1 in tibial pseudarthrosis. *Am J Hum Genet.* 2006;79(1):143-8.

35. Kang H, Jha S, Deng Z, Fratzl-Zelman N, Cabral WA, Ivovic A, et al. Somatic activating mutations in MAP2K1 cause melorheostosis. *Nat Commun.* 2018;9(1):1390.

36. Shah H, Joseph B, Nair BVS, Kotian DB, Choi IH, Richards BS, et al. What Factors Influence Union and Refracture of Congenital Pseudarthrosis of the Tibia? A Multicenter Long-term Study. *J Pediatr Orthop.* 2018;38(6):e332-e7.

37. Ono K, Karolak MR, Ndong Jde L, Wang W, Yang X, and Elefteriou F. The ras-GTPase activity of neurofibromin restrains ERK-dependent FGFR signaling during endochondral bone formation. *Hum Mol Genet.* 2013;22(15):3048-62.

38. Wang W, Nyman JS, Ono K, Stevenson DA, Yang X, and Elefteriou F. Mice lacking Nf1 in osteochondroprogenitor cells display skeletal dysplasia similar to patients with neurofibromatosis type I. *Hum Mol Genet.* 2011;20(20):3910-24.

39. de la Croix Ndong J, Stevens DM, Vignaux G, Uppuganti S, Perrien DS, Yang X, et al. Combined MEK inhibition and BMP2 treatment promotes osteoblast differentiation and bone healing in Nf1Osx -/- mice. *J Bone Miner Res.* 2015;30(1):55-63.

40. Lindsley A, Snider P, Zhou H, Rogers R, Wang J, Olaopa M, et al. Identification and characterization of a novel Schwann and outflow tract endocardial cushion lineage-restricted periostin enhancer. *Dev Biol.* 2007;307(2):340-55.

41. Huh CG, Factor VM, Sanchez A, Uchida K, Conner EA, and Thorgeirsson SS. Hepatocyte growth factor/c-met signaling pathway is required for efficient liver regeneration and repair. *Proc Natl Acad Sci U S A.* 2004;101(13):4477-82.

42. Duchamp de Lageneste O, Julien A, Abou-Khalil R, Frangi G, Carvalho C, Cagnard N, et al. Periosteum contains skeletal stem cells with high bone regenerative potential controlled by Periostin. *Nat Commun.* 2018;9(1):773.

43. Bouxsein ML, Boyd SK, Christiansen BA, Guldberg RE, Jepsen KJ, and Muller R. Guidelines for assessment of bone microstructure in rodents using micro-computed tomography. *J Bone Miner Res.* 2010;25(7):1468-86.

44. Fowlkes JL, Bunn RC, Ray PD, Kalaitzoglou E, Uppuganti S, Unal M, et al. Constitutive activation of MEK1 in osteoprogenitors increases strength of bone despite impairing mineralization. *Bone.* 2020;130:115106.

45. Creecy A, Uppuganti S, Girard MR, Schlunk SG, Amah C, Granke M, et al. The age-related decrease in material properties of BALB/c mouse long bones involves alterations to the extracellular matrix. *Bone.* 2020;130:115126.